Explicit Simulation of Cumulus Ensembles with the GATE Phase III Data: Comparison with Observations

KUAN-MAN XU AND DAVID A. RANDALL

Department of Atmospheric Science, Colorado State University, Fort Collins, Colorado

(Manuscript received 28 July 1995, in final form 29 May 1996)

ABSTRACT

The macroscopic behavior of cumulus convection and its mesoscale organization during Phase III of the Global Atmospheric Research Program's (GARP) Atlantic Tropical Experiment (GATE) is simulated with a two-dimensional (2D) cloud ensemble model. The model includes a three-phase bulk microphysics parameterization, a third-moment turbulence closure and an interactive, radiative transfer parameterization. The observed large-scale, horizontal advective effects and large-scale vertical velocity are imposed on the model's thermodynamic equations uniformly in the horizontal. The simulated, domain-averaged horizontal wind components are nudged toward the observed winds.

A detailed comparison with available observations is made in this study. The observed time variations of the surface precipitation rate, surface evaporation rate, outgoing longwave radiation flux, and the vertical distributions of temperature, water vapor mixing ratio, and relative humidity are successfully reproduced by the model, as well as the vertical structure and time evolution of major convective systems. The most significant result is that the model is able to reproduce the negative correlation between the intensity of convection and the convective available potential energy. The simulated total cloud amount compares favorably with the whole-sky camera observations of Holle et al., but the low-level cloud amount is significantly underestimated. In spite of its success, sensitivity tests suggest that the 2D model has stronger inhibiting effects on convection and is more efficient in vertical transports than is observed when the vertical wind shear is strong. The CEM also produces smaller amplitudes of the daily fluctuations in cloud amount and precipitable water than observed, due possibly to the shortcomings of the microphysics parameterization.

1. Introduction

The Global Atmospheric Research Program's (GARP) Atlantic Tropical Experiment (GATE) was one of the largest field experiments in meteorological history. It was conducted in the summer of 1974 (Kuettner and Parker 1976). One of the central objectives of GATE was to understand the scale interactions between convective activity and large-scale weather systems (ICSU/WMO 1972), that is, to better understand the mechanism or mechanisms by which deep cumulus convection is organized by the synoptic or large-scale motions and how the resulting convective activity affects the synoptic motions that can be resolved in large-scale models. Satellite, radar, aircraft, and highly-resolved upper air balloon observations were combined to extensively probe the convective cloud fields in the GATE area (Fig. 1), which was nested within two large arrays consisting of ships stretched across the tropical Atlantic Ocean. Supplemental observations such as surface-based cloud photography and boundary layer measurements were also used. The principal findings of the experiment were summarized in a seminar proceedings (NRC 1980). Houze and Betts (1981) later reviewed various aspects of observed convection and convective organization in the GATE area. The bulk effects of cloud ensembles on the large-scale circulation and their parameterization are the focus of this study.

One of the objectives of GATE was to estimate observationally the bulk effects of cloud ensembles on the large-scale circulation. Such an objective can be achieved with the diagnostic approach as first developed by Yanai et al. (1973), which can yield in-cloud information from given rawinsonde data. In the diagnostic studies, the net effects of all cloud-scale processes are estimated as residuals in the thermodynamic, momentum, and vorticity budget equations. In the thermodynamic budgets, these residuals are called the apparent heat source (Q_1) and apparent moisture sink (Q_2) (Yanai et al. 1973). With the use of a statistically steady cloud model for updrafts/downdrafts, the variables representing the properties of a cumulus ensemble, such as the cumulus mass flux and the eddy transports of heat and moisture, can be inferred by considering the balance of mass, heat, moisture, and possibly

Corresponding author address: Dr. Kuan-Man Xu, Department of Atmospheric Science, Colorado State University, Fort Collins, CO 80523.
E-mail: kmxu@cumulus.atmos.colostate.edu

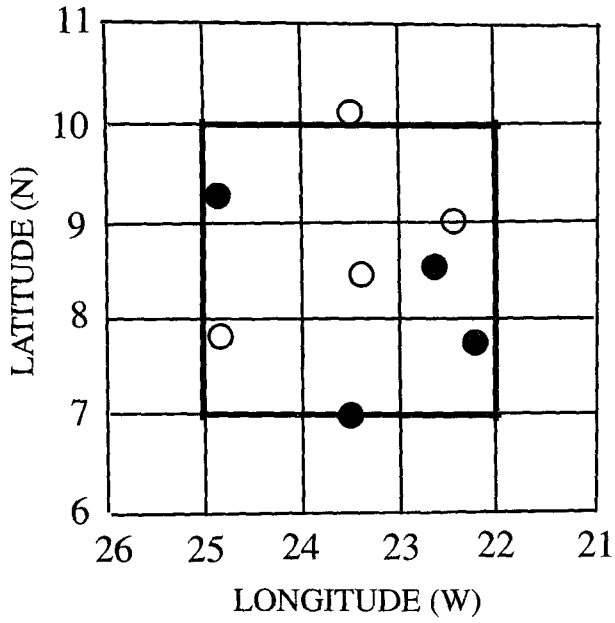

FIG. 1. The location of GATE area with B/C-array ships as indicated by open and closed circles. The closed circles denote ships providing cloudiness data. The heavy lines indicates the 3 × 3 area over which the observed large-scale data are averaged.

momentum between the cumulus ensemble and the large-scale environment.

The mechanisms of cumulus–environment interactions known from pre-GATE studies (Yanai et al. 1973; Ogura and Cho 1973) are as follows. The cumulus mass flux (M_c) exceeds the large-scale vertical mass flux; thus, it causes a compensating sinking motion between active clouds, that is, environmental subsidence. This cumulus-induced subsidence results in adiabatic heating and drying of the environment. On the other hand, the reevaporation of liquid water detrained from the clouds counteracts the heating and drying induced by the subsidence. This is especially true for the shallow clouds that detrain in the lower troposphere. See Yanai and Johnson (1993) for a detailed review.

The inclusion of the effects of downdrafts and mesoscale processes in diagnostic studies is a main area of research using the GATE data (e.g., Johnson 1976; Houze 1982; Cheng 1989a,b; Cheng and Yanai 1989). The inclusion of downdraft effects generally reduces M_c and thus reduces cumulus heating and drying in the lower troposphere (Johnson 1976; Cheng 1989b). Johnson (1976) attached each updraft to an "inverted" plume (a downdraft) by specifying a coefficient of proportionality that relates downdraft mass flux to updraft mass flux. Cheng's (1989a) convective-scale downdraft model considered the rainwater and vertical-momentum budgets of a tilted updraft. The rainwater flux from an updraft was the main mechanism for initiating a downdraft. Cheng (1989b) found that (i) the inclusion of convective-scale downdrafts is essential in order to obtain the effect of cumulus convection in budget calculations; (ii) convective-scale downdrafts tend to cool and moisten the lower cloud layer; and (iii) significant downdraft activity is usually associated with mesoscale convective systems (MCSs).

The inclusion of mesoscale effects in diagnostic studies is still rudimentary. Leary and Houze (1980) showed that the inclusion of anvil updrafts and downdrafts significantly changed the diagnosed profiles of convective mass and heat transports. Houze (1982) presented a diagnostic study on the heat budget of anvil clouds. He showed that the eddy transports in the heat budget are less important, but not negligible, while condensation/evaporation due to mesoscale updrafts/downdrafts are very important. Cheng and Yanai (1989) partially agreed with Houze (1982), but they argued that the eddy transports can be neglected in the anvil regions compared to the net condensation rate. This point of view was partially supported by Johnson and Young (1983) and Gallus and Johnson (1991), who diagnosed the heat and moisture budgets of the anvil regions of MCSs in the Tropics and midlatitudes, respectively. Tao et al. (1993), however, found that the eddy moisture transports are very important in both convective and anvil regions of simulated MCSs. Xu (1995) further demonstrated with simulated data that condensation/evaporation due to mesoscale motions, eddy transports and radiative effects are more or less equally important in the heat and moisture budgets of anvil regions.

Another objective of GATE is the testing of cumulus parameterizations. A commonly adopted method is the "semiprognostic" test, which is a one-step prediction of the cumulus activity based on given large-scale conditions such as advections of heat and moisture, turbulence fluxes, and radiative heating. The semiprognostic test was first proposed by Lord (1982) who tested the original Arakawa–Schubert (1974, hereafter A–S) parameterization using the GATE Phase III dataset. Krishnamurti et al. (1980) also tested the moist-convective adjustment (Manabe et al. 1965) and the Kuo (1965, 1974) schemes using the same dataset. They pointed out that the original moist-convective adjustment scheme overestimates the precipitation rate by an order of magnitude and produces excessive cooling and drying. The original Kuo scheme underestimates the precipitation rate and produces too much moistening but not enough heating.

Lord (1982) provided a detailed test of several important components of the A–S parameterization. He found that the predicted precipitation rates are highly correlated with the observed estimates and are well within observational uncertainty in both disturbed and undisturbed conditions. The vertical profiles of Q_1 and Q_2 are, however, overestimated in the lower troposphere. The overestimate is due partly to the lack of

downdrafts in the parameterization (e.g., Cheng and Arakawa 1990).

Another way to test cumulus parameterizations is through the explicit simulation of cumulus ensembles (Soong and Tao 1980). The simulated properties of cumulus ensembles can be directly compared with those obtained from a cumulus parameterization. Xu and Arakawa (1992) further applied this approach to test the sensitivity of the A–S cumulus parameterization to the horizontal resolution of large-scale models. A similar but more direct testing method is single-column modeling (Betts and Miller 1986; Randall et al. 1996). It is similar to the semiprognostic method but allows feedback from one time step to the next.

One of the principal findings summarized in NRC (1980) is "models that simulate the detailed life cycles of whole populations of clouds have begun to appear. Since they allow for large-scale forcing mechanisms to be externally specified, such models are powerful tools in the effort to understand how large-scale processes control a cloud ensemble." The models referred in this finding are called "cloud ensemble models" (CEMs) (e.g., Soong and Tao 1980; Krueger 1988). A CEM resolves individual clouds and their mesoscale organization but covers a large horizontal domain. It allows several clouds of various sizes to develop simultaneously and randomly within the model domain.

Soong and Tao (1980) specified the large-scale vertical velocity and the horizontal advective effects in their two-dimensional (2D) CEM simulation of one specific case during GATE, using a domain size of 64 km. More recent studies were also focused on individual or composited cases observed during GATE (e.g., Tao and Soong 1986; Tao et al. 1987; Lipps and Helmer 1986; Krueger 1988; Gregory and Miller 1989) using two- or three-dimensional models. Statistical properties of cumulus ensembles have been examined in these studies.

There is no single study that simulates the *entire* length of GATE Phase III with a CEM, however. The present study intends to do this. A similar study is being undertaken at the University of California, Los Angeles (UCLA) by C. Lin and A. Arakawa (1996, personal communication) for studying cumulus entrainment processes. They nudge the simulated domain-averaged temperature and water vapor mixing toward the observed ones. Grabowski et al. (1996) simulated only the first seven days of GATE Phase III. The main objective of the present study is to investigate the ability of a CEM to simulate the statistical properties of cumulus ensembles with observed large-scale data. This study is a first step in achieving the objectives of the Global Energy and Water Cycle Experiment's Cloud System Study (GCSS), which adopts CEM simulated datasets as test beds to develop cloud parameterizations for use in climate models (GCSS Science Team 1993). In this study, several sensitivity tests are also performed to address the limitations of the model.

2. Numerical simulations

The model used in this study is the two-dimensional (x and z) UCLA CEM. The details of the CEM have been described by Krueger (1988) and Xu and Krueger (1991). Briefly, the CEM is based on the anelastic system of dynamical equations with the Coriolis acceleration. The physical parameterizations of the model include 1) a third-moment turbulence closure (Krueger 1988), 2) a three-phase bulk cloud microphysics parameterization (Lin et al. 1983; Lord et al. 1984; Krueger et al. 1995), and 3) an interactive radiative transfer parameterization (Harshvardhan et al. 1987; Xu and Randall 1995a). The sophisticated turbulence parameterization consists of 35 prognostic equations for second and third moments, and a diagnostic equation for the turbulent length scale. The interactive radiative transfer parameterization is based on Harshvardhan et al.'s (1987) broadband radiative transfer model with cloud optical properties as formulated by Stephens et al. (1990). The details of the radiative transfer parameterization are described in Xu and Randall (1995a).

Other aspects of the model designs that may impact simulated results are (i) the periodic lateral-boundary conditions, (ii) the zero terminal velocity for ice crystals, (iii) the lack of horizontal advection of condensates, (iv) the lack of subgrid-scale cloudiness parameterization, (v) the method of prescribing large-scale advective effects, and (vi) the way of nudging the simulated, domain-averaged horizontal wind components toward the observed winds. The latter two are further explained below.

Because CEMs are designed to simulate the formation of an ensemble of cumulus clouds under given large-scale conditions, as if the CEM was situated within a grid box of a large-scale numerical model, information on large-scale destabilizing and moistening rates due to large-scale horizontal advection and large-scale vertical motion is imposed on the CEM grid points, uniformly in x. The horizontally uniform, large-scale, horizontal advective cooling and moistening rates, and vertical velocity observed during Phase III of GATE, $-(\partial\bar{\theta}/\partial t)_H$, $-(\partial\bar{q}_v/\partial t)_H$, and $\bar{W}$, where $\bar{\theta}$ is the potential temperature and q_v the water-vapor mixing ratio, are prescribed in all simulations described later. That is, $-(\partial\bar{\theta}/\partial t)_H$, $-(\partial\bar{q}_v/\partial t)_H$, and advection due to $\bar{W}$ are added to the right-hand sides of the perturbation equations of θ and q_v, respectively. This method is slightly different from the methods used in Xu et al. (1992), in which either $\bar{W}$ or the total advective effect is prescribed. It allows the horizontal inhomogeneity of the large-scale vertical advection, as in the real atmosphere. The domain-averaged vertical advective effects could, however, differ from observed if the model produces unrealistically large vertical gradients of domain-averaged temperature and moisture. Thus, a stricter evaluation of the performance of a CEM can be

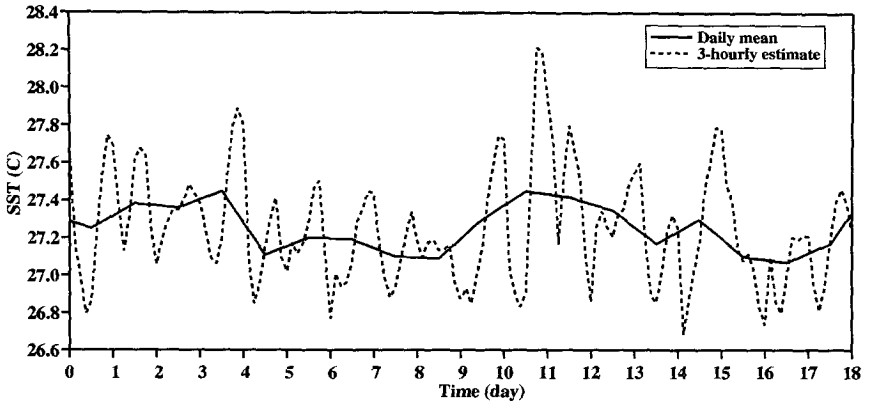

FIG. 2. Time sequence of observed daily mean sea surface temperature (solid line) from Krishnamurti et al. (1976) and 3-hourly estimated sea surface temperature. The time axis is from 1 to 18 September 1974.

achieved with the present method than that by prescribing the total advective effects.

Another variable prescribed in the CEM is the horizontal pressure gradient; the observed wind components are used to approximate the horizontal pressure gradients through the geostrophic wind relation due to the lack of observed data. Even if the observed horizontal pressure gradients were available, it would not be possible to predict the domain-averaged horizontal wind components in the CEM correctly without the information on the advective tendency of wind components. Incorrect profiles of large-scale wind components will affect the simulated structures of cloud systems. To overcome this problem, an extra term is added to each of the horizontal wind component equations; that is,

$$\frac{\partial u}{\partial t} = \cdots - (\bar{u} - u_{\text{obs}})/\tau \qquad (1)$$

$$\frac{\partial v}{\partial t} = \cdots - (\bar{v} - v_{\text{obs}})/\tau, \qquad (2)$$

where $\bar{u}$ and $\bar{v}$ are the domain-averaged wind components, u_{obs} and v_{obs} are the observed wind components, and τ is the nudging timescale. Such a procedure forces the simulated domain-averaged wind components to be very close to the observed ones if τ is small. The horizontal inhomogeneity of u and v inside the domain is preserved by the nudging procedure, however. This is because the nudging terms in (1) and (2) are not functions of x. If the domain-averaged wind components are forced to be equal to the observed ones without the nudging procedure, a simulation can break up after a few hours. We choose τ to be 1 hour in the simulations.

The control simulation, called G, was run for 18 days of physical time, from 1 to 18 September 1974, with a time step of 10 s. The Thompson et al. (1979) dataset, as described in section 3, is used to provide information on $-(\partial\bar{\theta}/\partial t)_H$, $-(\partial\bar{q}_v/\partial t)_H$ and $\bar{W}$ in all simulations described below except for O. The observed, daily mean sea surface temperature (SST; Krishnurmuti et al. 1976) is used in all simulations except for T and CT (Fig. 2); the diurnal variation of SST cannot be incorporated into the simulation because it is not available. However, an attempt has been made to estimate the diurnal variation of SST based on the observed surface sensible heat flux, surface wind speed, and surface air temperature using the bulk aerodynamic formula. The magnitude of the diurnal variation of SST is less than 1 K (Fig. 2), which is consistent with limited observations (Ostapoff 1977). Incorporating such diurnally varying SST could slightly improve the simulated results. This will be discussed in a sensitivity test, called T, which includes the estimated diurnally varying SST shown in Fig. 2. Sensitivity test CT is performed with a constant SST of 300.965 K, which is about 0.5 K higher than the observed 18-day mean (Fig. 2). Another sensitivity test, called S, is performed with height-independent wind components, which are equal to the surface values used in G. In such a test, the surface sensible and latent heat fluxes are approximately equal to those in G. Furthermore, the horizontal advective effects are assumed to be identical to those in G, although the horizontal wind components are altered. The sensitivity tests T and S were only run for the first six days, as explained below, due to the enormous computing time required. Test O is identical to G except for using the Ooyama dataset to provide information on the total advective effects and the horizontal wind components (Esbensen and Ooyama 1983; Sui and Yanai 1986) so that some differences between G and observations can be explained by the insufficient quality of the Thompson et al. dataset. Table 1 summarizes the design of all simulations described above.

Each simulation except for CT and O consists of three experiments, two of them are initialized with perturbed initial conditions; simulations CT and O each consists of a single run. The vertical profiles of the

TABLE 1. A list of numerical simulations performed in this study.

Simulation	Length	Ensemble of experiments	SST	Large-scale forcing	Wind profiles
G (control)	18 days	Yes	Daily mean	Thompson et al.	Observed
T	6 days	Yes	Diurnally varying	Thompson et al.	Observed
S	6 days	Yes	Daily mean	Thompson et al.	Nonsheared
CT	18 days	Single run	300.965 K	Thompson et al.	Observed
O	18 days	Single run	Daily mean	Ooyama	Observed

initial perturbations of temperature and water vapor mixing ratio are shown in Fig. 3. The perturbations are very large at selected levels. In the results shown later, an average of the three experiments is used to represent a simulation. Such an ensemble of experiments for each simulation results in enormous computing cost. Ideally, many more experiments should be performed with different profiles and/or magnitudes of the perturbations. The standard deviations of temperature and water vapor mixing ratio between perturbed and unperturbed experiments for G are shown in Fig. 3. Both variables are first averaged over the entire domain and 3 h in time. These deviations should give a measure against which we can judge the significance of the differences between simulation and observation and between G and the sensitivity tests.

The remaining aspects of the simulations are identical to those described in earlier studies with the UCLA CEM (Xu and Krueger 1991; Xu et al. 1992). For example, the domain size is 512 km, with a horizontal grid size of 2 km. The vertical coordinate is stretched to give finer resolution near the surface, with 33 layers. The radiation module is called every 150 s using the "accumulated" method proposed by Xu and Randall (1995a).

3. The GATE dataset

The GATE sounding data used in this study except for sensitivity test O are those described by Thompson et al. (1979). The dataset was kindly provided by Professor R. Reed's group at the University of Washington. The variables include the temperature, water vapor mixing ratio, horizontal wind components, and vertical velocity for the B-scale area (Fig. 4) with a 3-h interval between observations. The original data were analyzed with use of the method of least squares. Data within approximately ±6 h of the given hour t were employed in the fitting. The horizontal advective cooling and moistening rates are available (Fig. 5). The horizontal

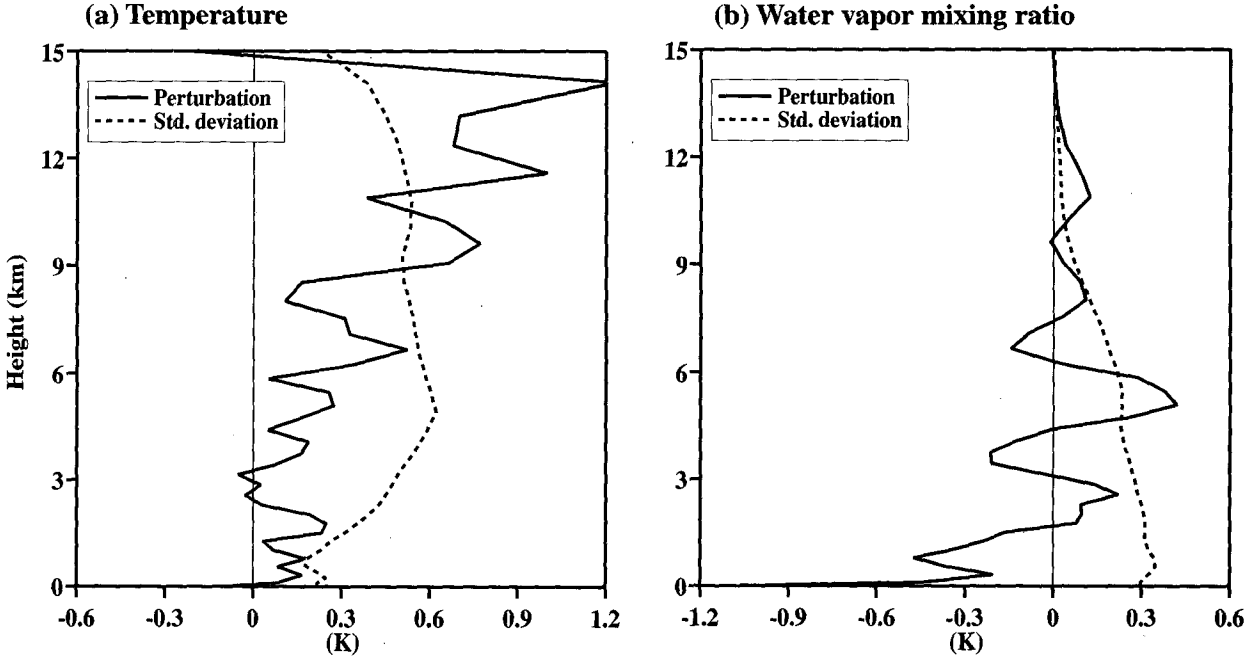

FIG. 3. Vertical profiles of (a) temperature and (b) water vapor mixing ratio perturbations for the perturbed experiments and standard deviations between perturbed and unperturbed experiments.

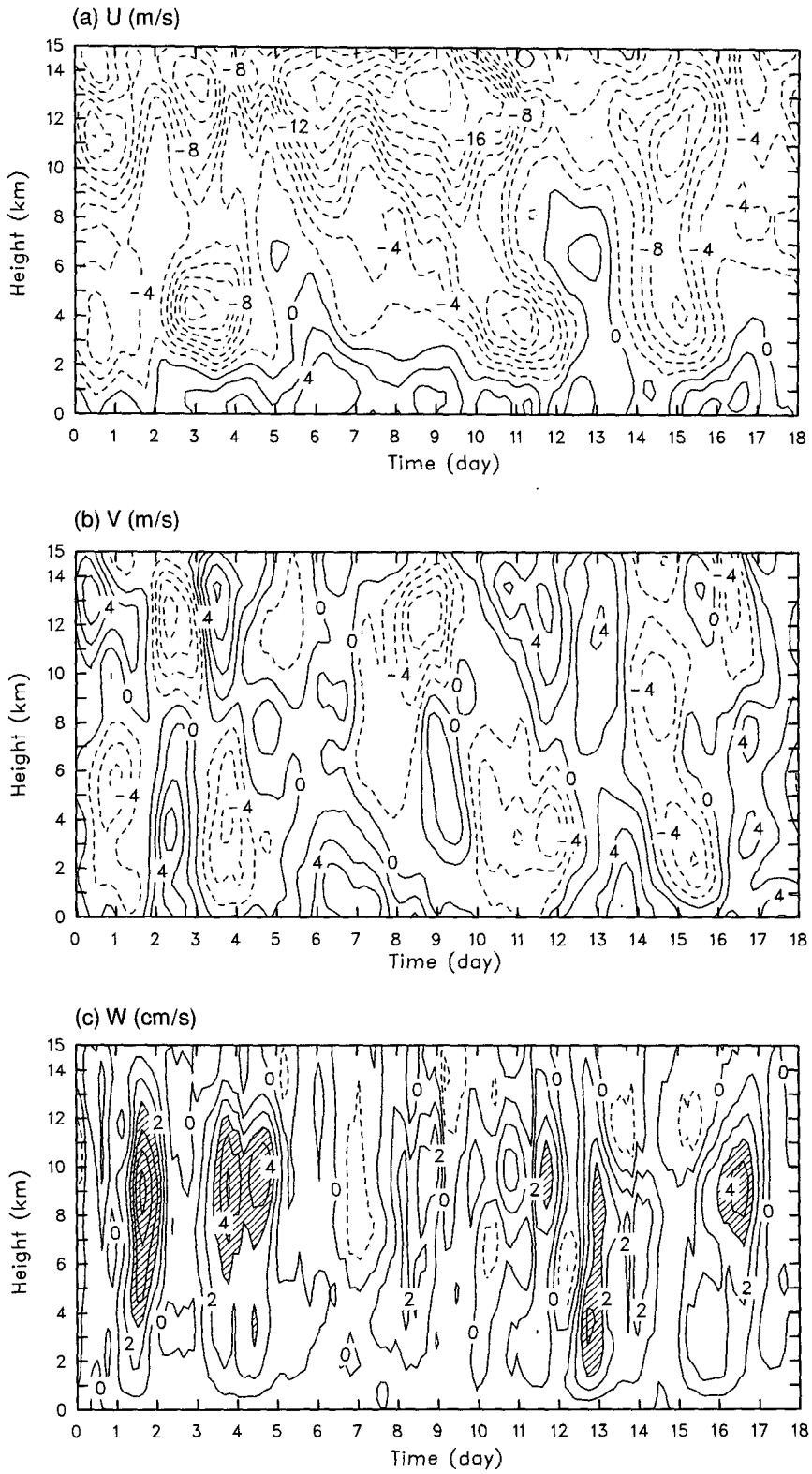

FIG. 4. Time–height cross sections of (a) x-component velocity, (b) y-component velocity, and (c) vertical velocity. The contour interval is 2 m s^{-1} in (a) and (b). The contour interval in (c) is 1 cm s^{-1}, with contours over 3 cm s^{-1} hatched.

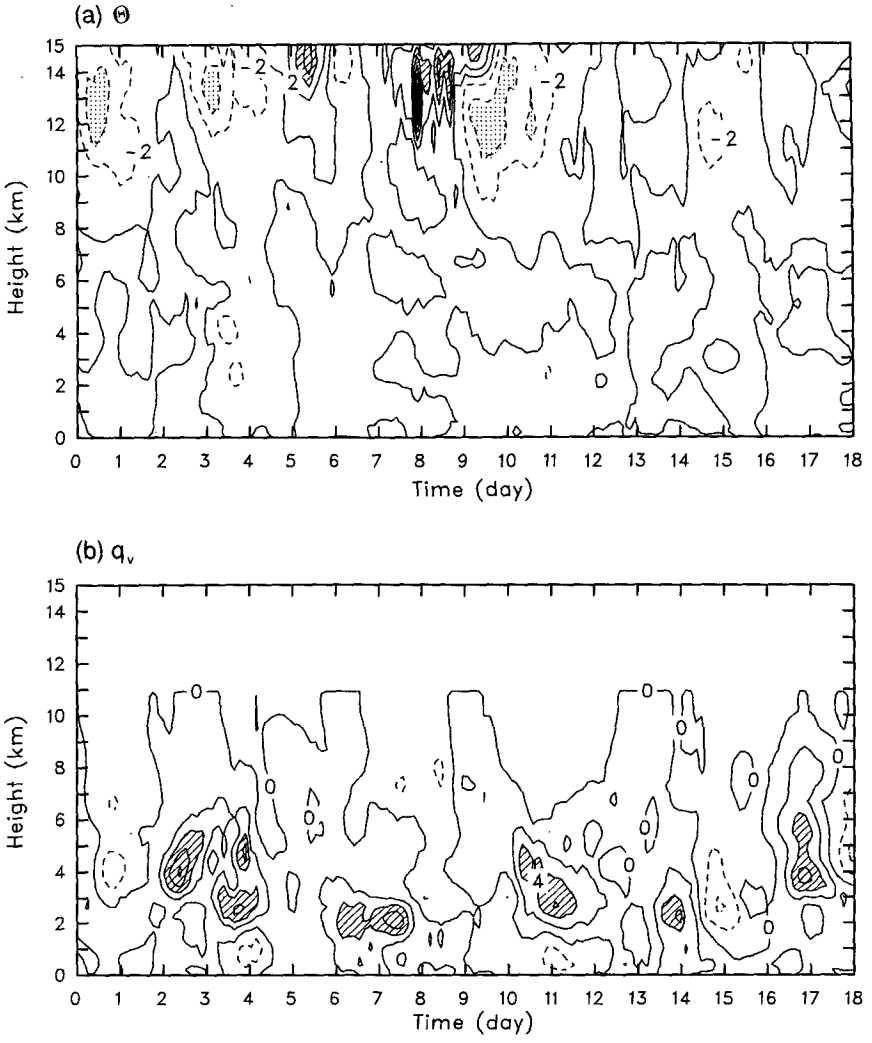

FIG. 5. Time–height cross sections of the observed horizontal advection of (a) potential temperature and (b) water vapor mixing ratio. The contour interval is 1 K day^{-1}. Contours over 4 K day^{-1} are hatched. Contours less than −4 K day^{-1} are dotted.

advection of potential temperature (Fig. 5a) was generally very small (<2 K day^{-1}) except in the upper troposphere. Large magnitudes of the horizontal advection of water vapor mixing ratio occurred mainly in the lower and middle troposphere (Fig. 5b).

Variables used for verification of the simulations are (i) 3-hourly surface precipitation rate derived from radar observations (Hudlow and Patterson 1979); (ii) 3-hourly surface sensible heat flux; (iii) 3-hourly surface latent heat fluxes; (iv) 3-hourly radiative heating rates (Cox and Griffith 1979); (v) the daytime hourly cloud amounts for selected layers (Holle et al. 1979); and (vi) the hourly outgoing longwave radiation flux (Murakami 1979). The sensible and latent heat flux data (Thompson et al. 1979) were obtained by the bulk aerodynamic method using the mean hourly wind, temperature, and humidity measurements from the booms of four B-scale ships (solid circles in Fig. 1). They were then smoothed over a 12-h period, in consistent with the approximately 12-h fitting interval employed in the sounding data.

The radiative heating rates are averaged over the B-scale area. They are based on the calculations performed by Cox and Griffith (1979) from compositing radiative divergence profiles on the basis of synoptic observations and satellite and radar inferred cloud structures. Two basic types of clouds were assumed in their calculations: thick clouds extending down from cloud top to 950 mb, and thin clouds confined within the same layer as the cloud top. Twenty-eight shortwave and twenty-five longwave radiative divergence profiles were used to determine the area-average radiative divergence by applying them over more homogeneous subareas. The size of the sub-area was deter-

mined by the spatial resolution of the satellite sensors. The thickness of the layer used in the calculation was 100 mb from 100 mb to 1012 mb, with an additional layer 12 mb thick near the surface.

The hourly low-level and total cloud amounts from whole-sky camera observations were based on data averaged from four U.S. ships (Holle et al. 1979). See Fig. 1 for the location of these four ships. The whole-sky camera observation of cloud amount is similar to that by a meteorological observer on the ground. This method of observation from a single point introduces two features differing from the calculation of cloudiness from the model: 1) a cloud overhead covers more area than one near the horizon, and 2) apparent cloudiness near the horizon can represent many more clouds than overhead (Holle et al. 1979). When there are clouds overhead, it is more likely that the cloud amount is overestimated because the viewing distance is shorter. Another factor is that the observed cloud amount does not well represent the mean over the B-scale area because the viewing areas between two cameras do not overlap and the cloud amount outside the B-scale area is also included. The cloud amount observations were available only for daytime. Information on other cloud types was also available, but the low-level and total cloud amounts were believed to be more reliable than the others (Holle et al. 1979).

4. Results

a. Basic features of the simulated convection

Several MCSs were observed during Phase III of GATE (Table 2; Houze and Betts 1981). They are classified as either fast-moving squall-type or slow-moving nonsquall-type according to the propagation speed of their leading convective lines (Barnes and Sieckman 1984). The fast-moving MCSs (4, 12, and 16 September) occurred when the low-level wind shear was very strong (Fig. 4a). The direction of propagation was parallel to the shear. The slow-moving MCSs (2, 5, 14, and 17 September) occurred when the low-level wind shear was significantly less. Their direction of propagation was normal to the shear. In addition, significant large-scale updrafts were associated with these MCSs (Fig. 4c). In this section, the temporal evolution and horizontal structures of simulated MCSs are presented, followed by the composite structures of three types of MCSs.

Figures 6, 7, and 8 show Hovmöller diagrams ($x - t$ sections) of surface precipitation rate, outgoing longwave radiation (OLR) flux, and cloud water + ice content, respectively. The time axis starts from 00Z 1 September to 24Z 18 September. Gross features of simulated convection are as follows. Fast-moving MCSs, slow-moving MCSs, and short-lived scattered systems are produced during the 18-day integration. The timing of fast- (4, 12, and 16 September) and slow-moving MCSs (2, 5, 14, and 17 September) is approximately consistent with observations (compare with Table 2, which is composited from a summary of the literature with the constraint that the MCSs were located within the B-scale array). Suppressed convection is well simulated on 1, 3, and 11 September but less well simulated on 7, 10, 15, and 18 September due to 1) the periodic lateral-boundary conditions, 2) the lack of horizontal advection of condensates, and 3) the time smoothing of large-scale forcing where 1) and 2) are related.

Simulated fast-moving MCSs last for long periods, typically between 12 and 24 h. Their propagation speed is approximately 10 m s^{-1}. Heavy precipitation associated with the MCSs is concentrated in a narrow band. The upper-tropospheric anvils associated with these MCSs are always located behind the leading convective lines (Fig. 7). This is partly related to the rapid westward propagation of the MCSs. The 4 September MCS occurs more than 6 h earlier than observed and dissipates earlier than observed (Table 2). This is partly due to the time smoothing used in analyzing the sounding data (Thompson et al. 1979). The earlier occurrence is also related to the influence of a slow-moving MCS propagating into the south part of the B-array (Arkell and Hudlow 1977). The CEM, however, cannot distinguish these two systems. The 12 and 16 September MCSs are also well simulated except for slightly weaker strength of 12 September MCS. The reason for the more successful simulation of fast-moving MCSs is that the low-level wind shear is approximately parallel to the direction of propagation of MCSs in the 2D model.

TABLE 2. Major mesoscale convective systems occurring during Phase III of GATE.

Time period from	Time period to	Propagation speed and direction	Study
1100 UTC 2 Sep	2300 UTC 2 Sep	6 m s^{-1}, S	Mower (1977)
1200 UTC 4 Sep	0300 UTC 5 Sep	12 m s^{-1}, SW	Houze (1977)
0300 UTC 5 Sep	2100 UTC 5 Sep	3 m s^{-1}, SW	Leary and Houze (1979); Leary (1979)
1100 UTC 12 Sep	1800 UTC 12 Sep	13.5 m s^{-1}, SW	Gamache and Houze (1982)
0900 UTC 14 Sep	2400 UTC 14 Sep	2.5 m s^{-1}, E	Zipser et al. (1981)
0600 UTC 16 Sep	2100 UTC 16 Sep	5 m s^{-1}, S	Mansfield (1977)
2100 UTC 16 Sep	1200 UTC 17 Sep	not available	Tollerud et al. (1985)

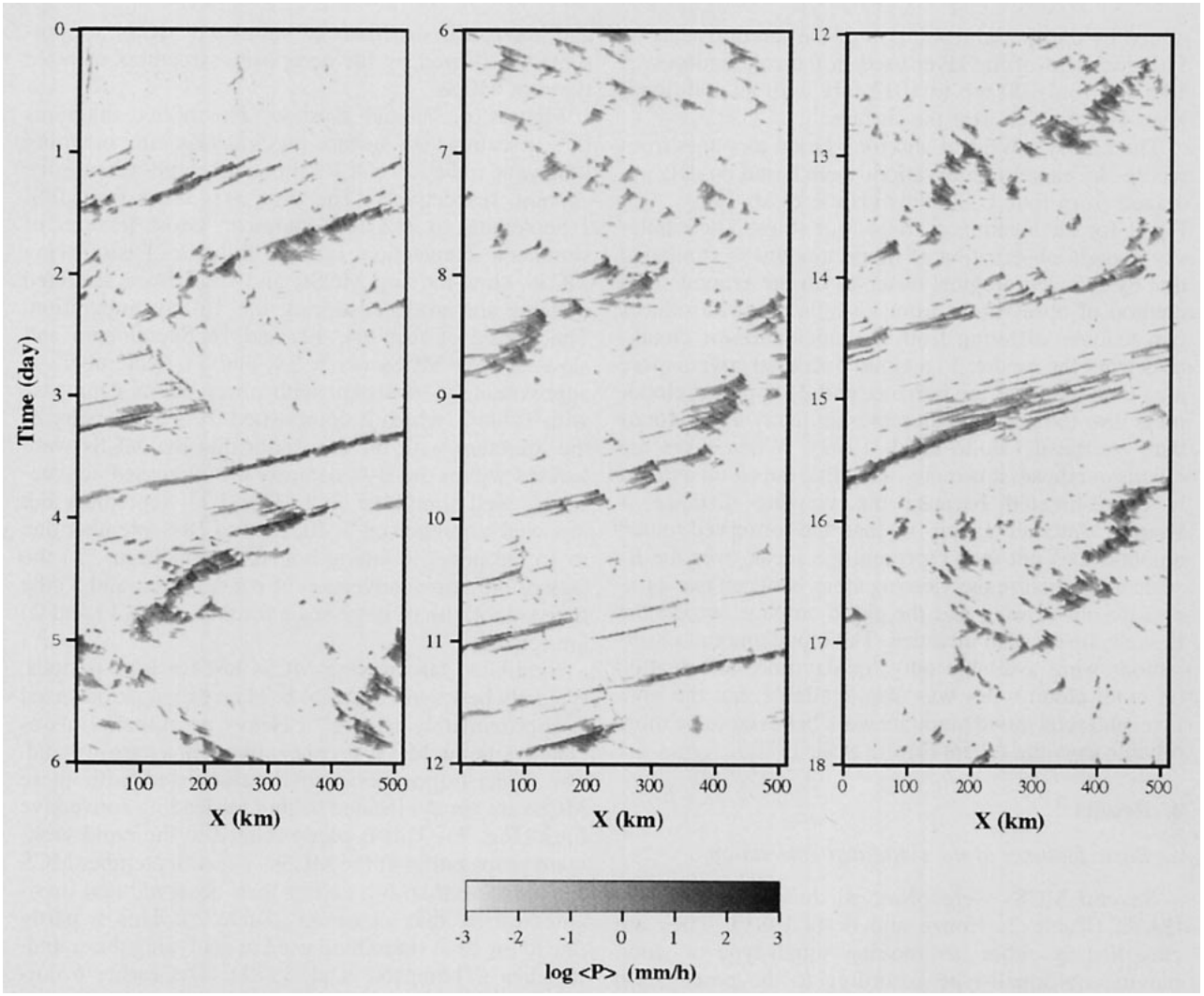

FIG. 6. Hovmöller diagrams ($x - t$ sections) of surface precipitation rate, based on 15-min averages from the unperturbed experiment of simulation G. The logarithm of surface precipitation rate is indicated by a linear grayscale: white represents 0.001 mm h^{-1}; black: 1000 mm h^{-1}.

Simulated slow-moving MCSs differ from fast-moving ones mainly in that (i) their propagation speed is much slower, typically 2–5 m s^{-1}; (ii) the MCSs last for less than 12 h; (iii) upper-tropospheric anvils can sometimes occur ahead of the leading convective lines (Fig. 7); and (iv) the relatively heavy surface precipitation is spread over a wider region (e.g., comparing 5 September with 4 September MCSs). The first three results are consistent with observations (e.g., Houze and Betts 1981). The last result may not agree with observations, depending the case (Zipser et al. 1981; LeMone et al. 1984b). The 2D CEM cannot simulate the orientation of slow-moving MCSs because the vertical wind shear cannot be normal to the direction of propagation. What probably happens is that the 2D model tries to simulate a less organized MCS under weak vertical x-component shear. This may explain the broad band of relatively heavy surface precipitation. It should be pointed out that the 14 September MCSs are well organized, but not as long-lived as observed. They are not as linearly organized as observed (Zipser et al. 1981), whereas the 5 September MCSs are more linearly organized than observed (Leary and Houze 1980). This is because the observed wind shear is mainly in the north–south direction on 14 September, but in the east–west direction on 5 September. The simulated MCS on 2 September moves more rapidly than other slow-moving MCSs. The observed fast propagation on 2 September is southward, not westward as simulated (Table 2). It also occurs earlier than observed and lasts longer than observed (Mower 1977).

As far as the surface precipitation is concerned, scattered convective systems often last for less than 6 h, and some only 1 to 2 h. As expected, the life cycles of

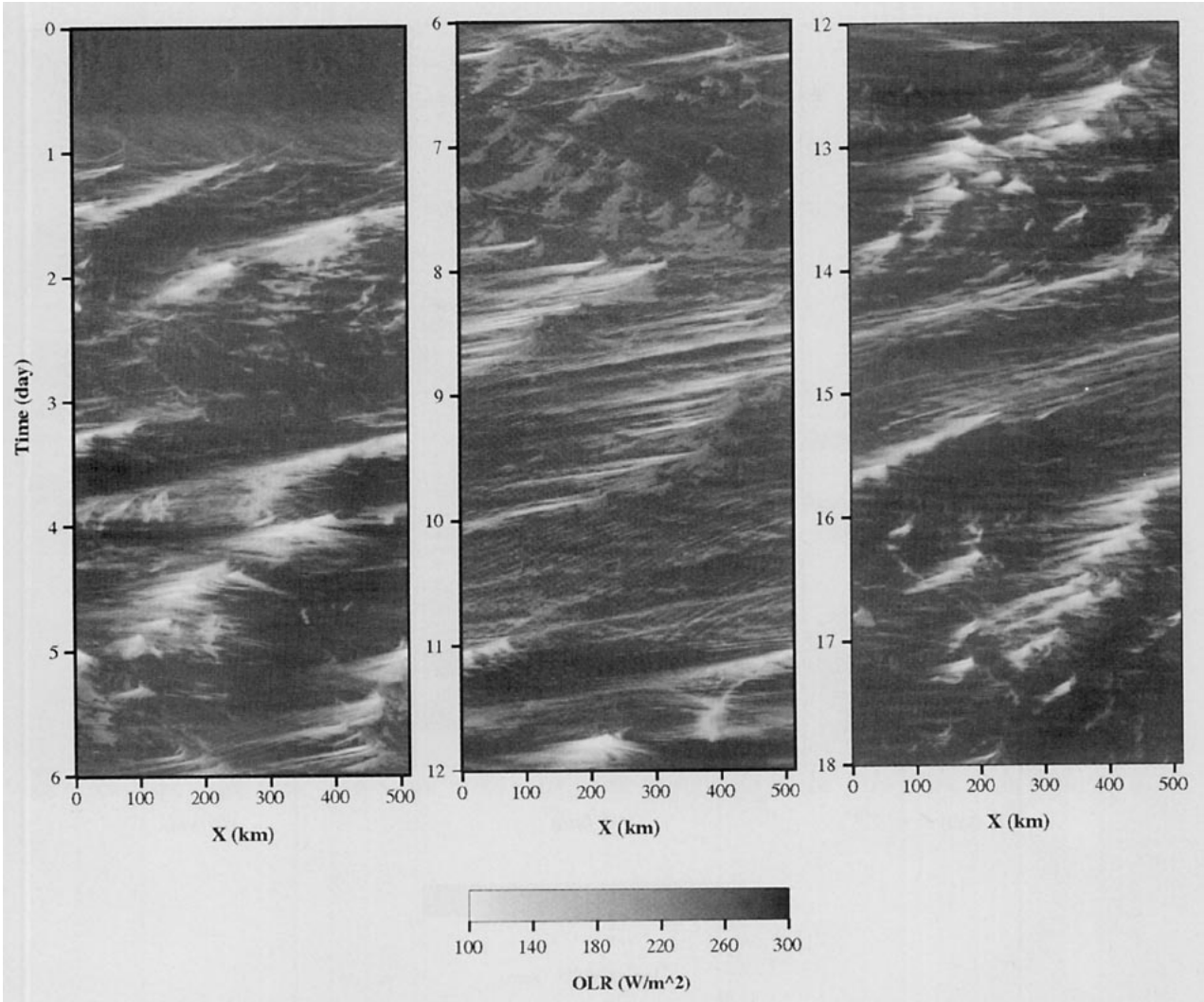

FIG. 7. Same as in Fig. 6 except for outgoing longwave radiation (OLR) fluxes. The OLR is indicated by a linear grayscale: white represents 100 W m^{-2}; black: 300 W m^{-2}.

these systems are much longer as seen from the OLR. There are several cloud systems within the domain at a given instant. A dissipating system can sometimes trigger a new one. For example, this happens on 8 September. The result was labeled as a slow-moving MCS by LeMone et al. (1984a). They mentioned, however, that the system was not well organized. Nevertheless, the surface precipitation rate associated with these systems is generally less than that of the well-organized systems discussed above. Most of the observed scattered systems on 6 and 7 September propagated eastward (Arkell and Hudlow 1977), as do the simulated ones.

The maximum horizontal extent of MCSs and the existence of widespread anvil clouds can be more clearly seen from the OLR (Fig. 7) than from the surface precipitation rates (Fig. 6). In the regions without anvil clouds, shallow clouds can be identified, most of which move in a direction opposite to major MCSs. During the periods without strong MCSs (e.g., 9 and 10 September), the high thin clouds drift with the mean large-scale flow. This may be caused by the large horizontal advective cooling above 12 km (Fig. 5a).

The thickness of clouds can be seen from the diagram of cloud water + ice content (Fig. 8). The convective lines associated with MCSs always have large integrated cloud water and ice contents. Along with Figs. 6 and 7, shallow clouds and isolated cloud cells can be identified. Shallow clouds generally propagate eastward due to the low-level westerlies (Fig. 4a). These clouds often form along gust fronts that propagate toward the east. In addition, Fig. 8 shows that there are many small dark dots, which are associated with isolated cloud cells. These cells cannot be identified in Fig. 7. The life spans and horizontal extents of these

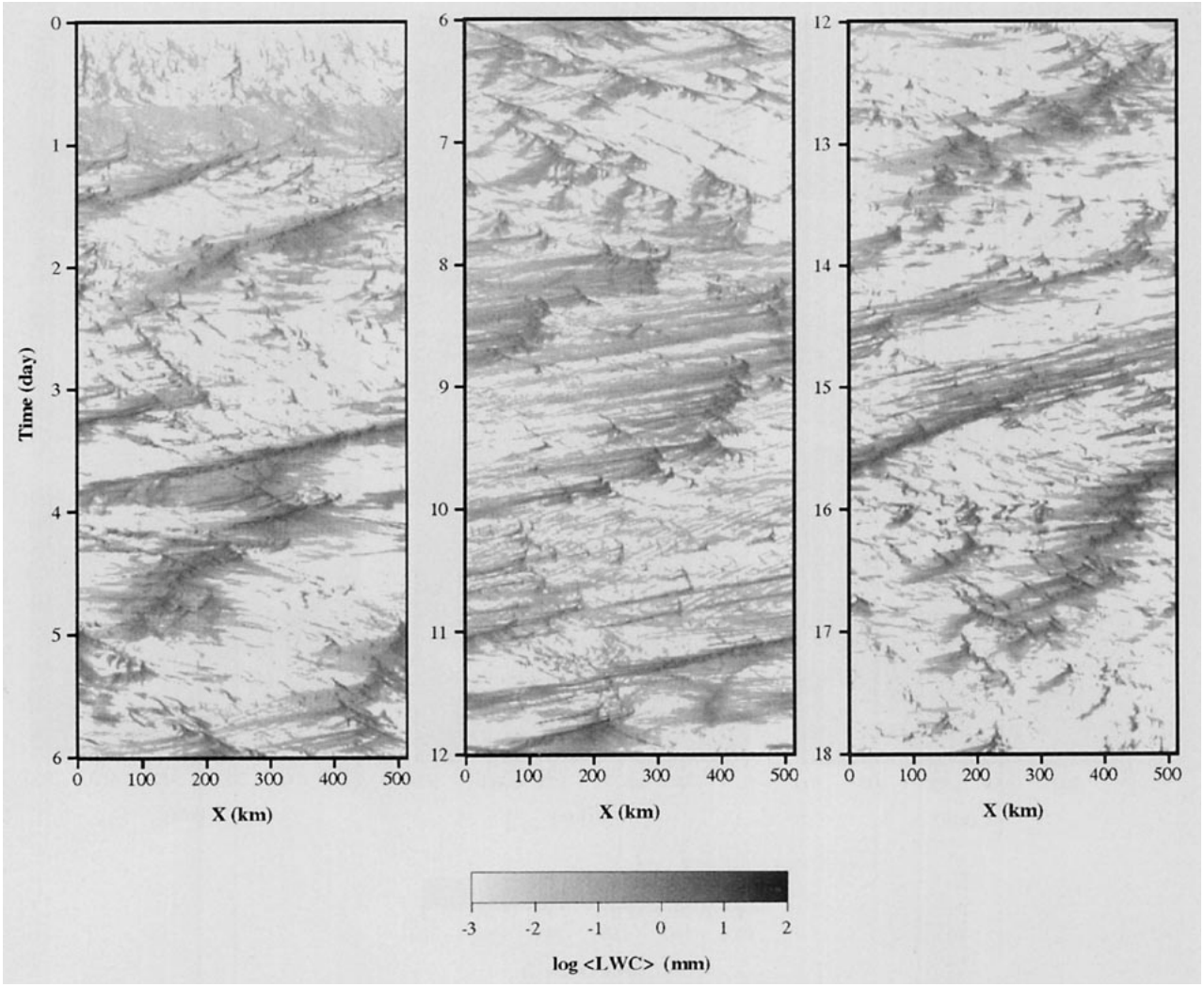

FIG. 8. Same as in Fig. 6 except for vertical integrals of cloud water and ice mixing ratios. The logarithm of liquid water content is indicated by a linear grayscale: white represents 0.001 mm; black: 100 mm.

cells are much shorter and smaller than those of the leading convective lines.

Next, the vertical structures of selected MCSs are presented as examples to illustrate the similarities and differences. The vertical velocity w, the total condensate mixing ratio q_t, the temperature deviation from the domain average θ', and the radiative heating rate Q_R are shown. A 4-h average is performed to give a composite structure with respect to the propagation speed of a MCS. That is, the grid is shifted horizontally according to the propagation speed before averaging.

Figure 9 shows a fast-moving MCS on 12 September, averaged from 0300 to 0700 UTC. The observed, composite structure of this MCS was analyzed by Gamache and Houze (1982, 1985). The propagation speed of the simulated MCS is -9.7 m s^{-1}. The MCS is characterized by a narrow (15 km wide) convective band and a rearward tilted anvil (90 km wide). A large amount of condensate occurs in the convective band, which is associated with strong vertical motions. On the other hand, there is a relative maximum of condensates between the 4- and 5-km levels behind the convective line, which is supposedly a melting band. There is a weak downward motion below the anvil and an upward motion above it. This is consistent with observations (Zipser 1977; Houze 1977; Gamache and Houze 1982). In addition, there are some weak shallow clouds ahead and behind the main system, as in the observations.

The temperature deviation of this MCS is characterized by a warm region in the upper-tropospheric anvil, a cold region just below the melting level, a slightly warm region between 1.5 and 3 km, and a cold subcloud layer below the anvil, which are respectively caused by the following processes: condensation/sublimation due to mesoscale lifting, cooling due to melt-

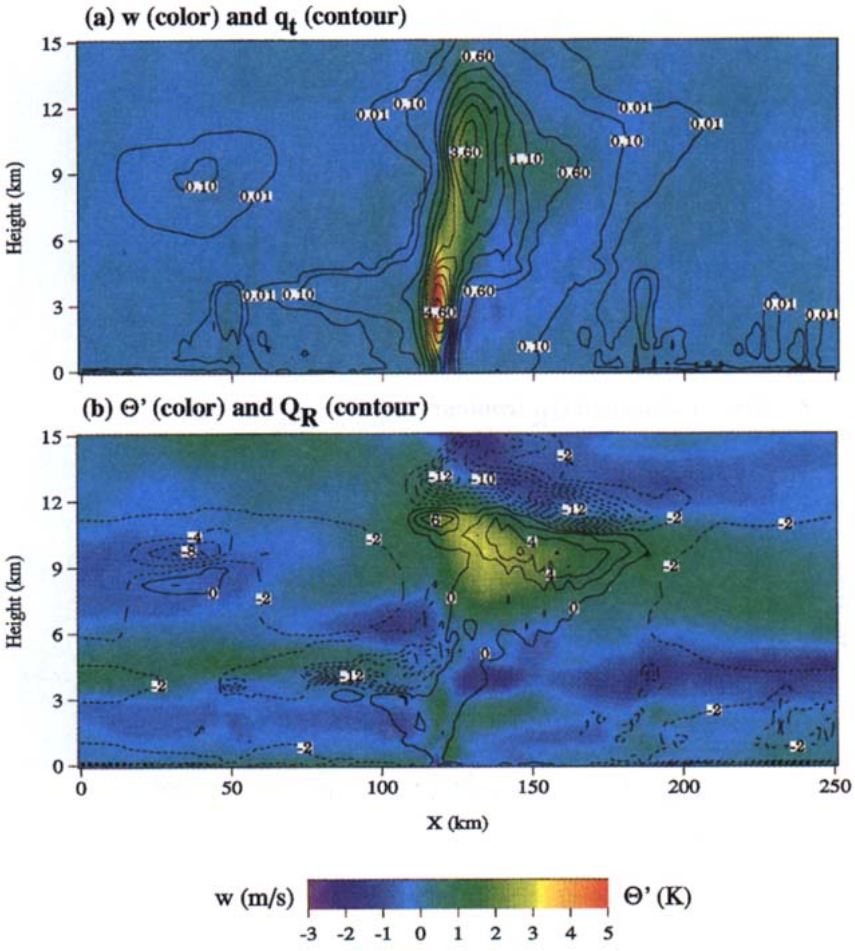

FIG. 9. The $x - z$ section of (a) vertical velocity (color), total condensate mixing ratio (contour), (b) potential temperature deviation from the domain (color), and radiative heating rate (contour) for a squall-type convective system on 12 September. The time average is from 0300 to 0700 UTC.

ing, warming due to mesoscale subsidence, and evaporative cooling of rainwater. Ahead of the leading convective line, there is warm air in the subcloud layer and near the melting level. Thus, the atmosphere between 2 km and the melting level is more stable than the domain average, which inhibits the shallow convection from penetrating to the upper troposphere. The features described above agree with those observed by Gamache and Houze (1982) except that the model results show more detailed spatial structures.

The radiative heating and cooling in the upper troposphere can also influence the temperature distribution, especially the large cloud-top cooling. (Note that solar radiation is absent during the averaging period.) The radiative warming inside the anvils is also important to the destabilization of the anvils (e.g., Webster and Stephens 1980; Xu and Randall 1995b), which enhances the circulations of the anvils.

Figure 10 shows a slow-moving MCS on 5 September, averaging from 1000 to 1400 UTC (0830 to 1230 local time). The propagation speed of this MCS is -3.7 m s^{-1}. The vertical structure differs from that of the fast-moving MCS discussed above in the following aspects: 1) the leading convective line is tilted westward; 2) the convective line is much wider; 3) the anvils surround the convective line; and 4) the radiative cooling above the anvil is much smaller, but the radiative heating inside the anvil is larger due to solar radiation. The temperature deviation is generally similar to that of the fast-moving MCS. The first two features may not be realistic, as mentioned earlier, due to the inability of 2D model to simulate the 3D nature of slow-moving MCSs and the upper-level wind shear.

Figure 11 shows two less-organized systems on 6 September, averaging from 0600 to 1000 UTC. The propagation speed of these systems is 2.5 m s^{-1}. Al-

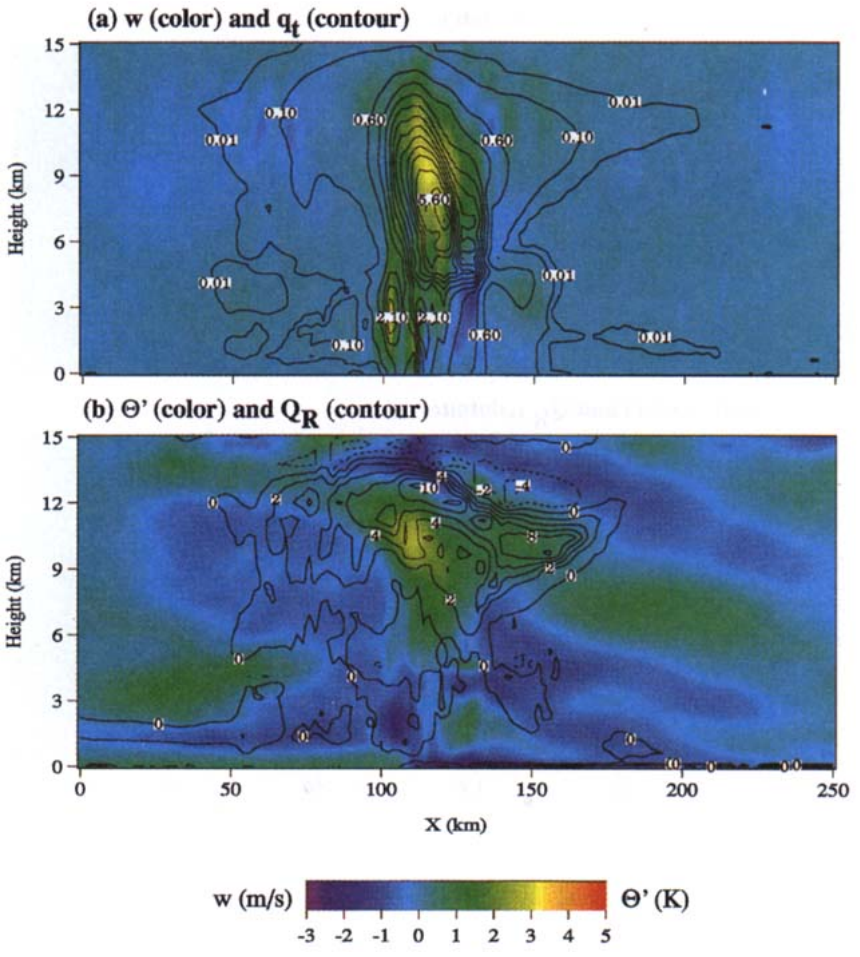

FIG. 10. Same as in Fig. 9 except for a nonsquall-type convective system on 5 September. The time average is from 1000 to 1400 UTC.

though the precipitating bands propagate eastward, the anvils associated with them drift westward with the large-scale flow. This produces a large westward tilting of the systems but not of the leading edge, especially the mature one on the left. The vertical velocity and q_t are much smaller than those of fast- and slow-moving MCSs (Figs. 9a and 10a) and θ' is not very large.

In summary, the detailed spatial structure and temporal evolution of the simulated MCSs have a fairly good correspondence with observations. The fast-moving MCSs are more successfully simulated than the slow-moving MCSs. Suppressed convection is well simulated on 1, 3, and 11 September. The highly three-dimensional nature of slow-moving MCSs obviously cannot be simulated (Mower 1977; Leary and Houze 1979; Zipser et al. 1981). The best that a 2D CEM can do is to capture the collective effects of MCSs on the large-scale thermodynamic budgets, which are discussed below.

b. *Comparison with observations*

Selected results from the control simulation G are presented in this section. Sensitivity tests will be presented in section 4c. All of the simulated variables shown below are averaged over the entire domain in space and over 3 h in time.

Figure 12a shows the time series of the observed and simulated surface precipitation rates. The observed precipitation rate was based on the average over the B-scale array in space, and over 3 h in time (Hudlow and Patterson 1979). A remarkable agreement between observation and simulation is readily seen in Fig. 12a, partly due to the fact that observed large-scale forcing is prescribed in the model. Some disagreements regarding the time evolution and the peak magnitude are, however, apparent. For example, there is a tendency for the simulated peaks to occur earlier than the observed ones before 13 September. The peaks appear rather flat on 2, 9, and 12 September. There are more

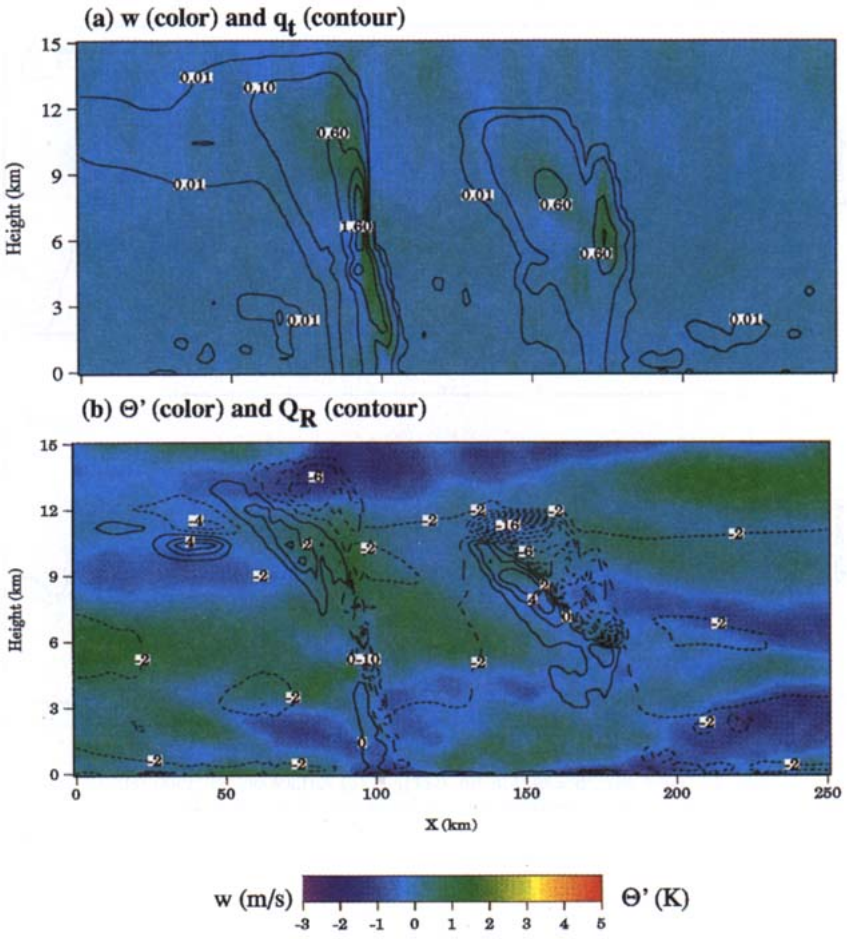

FIG. 11. Same as in Fig. 9 except for two scattered convective systems on 6 September. The time averaging is from 0600 to 1000 UTC.

high-frequency variations in the simulated surface precipitation rate, which is due to the lack of enough realization of ensemble simulation and possibly the diurnal variation of SST, as well as insufficient ensembles of clouds for a realization in a 2D model.

The agreement between the observed and simulated surface evaporation rates is excellent throughout the simulation (Fig. 12b). Small underestimates and overestimates are present. Most underestimates (overestimates) are related to those in the surface precipitation rate except for 9 September and the period after 13 September. Because the simulated, domain-averaged wind components are nudged toward the observed wind, the errors in the surface evaporation rate are largely related to those in the near-surface moisture and the lack of the diurnal variation of SST in the simulation.

Figure 13a shows the differences between the simulated and observed temperature. Most differences are between -1 K and $+1$ K in the lower and middle troposphere (up to 10 km) throughout the simulation. They are as high as $\pm 2-3$ K in the upper troposphere during some periods. Simulated temperature is mostly lower than observed in the first 10 days but mostly higher in the last 8 days, especially in the upper troposphere. It is not conclusive that there is a warming trend in the model because the simulated temperature on 15 and 16 September is lower than observed. Nevertheless, these large differences are statistically significant errors since they are, at least, twice as large as the standard deviations shown in Fig. 3a, which measure CEM's uncertainty due to errors in the initial condition.

The differences between the simulated and observed water vapor mixing ratios (Fig. 13b) are generally small except in the lower troposphere during some periods. These differences can be attributed to the lack of horizontal moisture advection in the lowest 2 km in the Thompson et al. dataset since the Ooyama dataset provides a much better simulation (see section 4c). Nevertheless, the largest differences (absolute values > 1.5 g kg^{-1}) appear only on 4, 8, 12, 15, and 18 September,

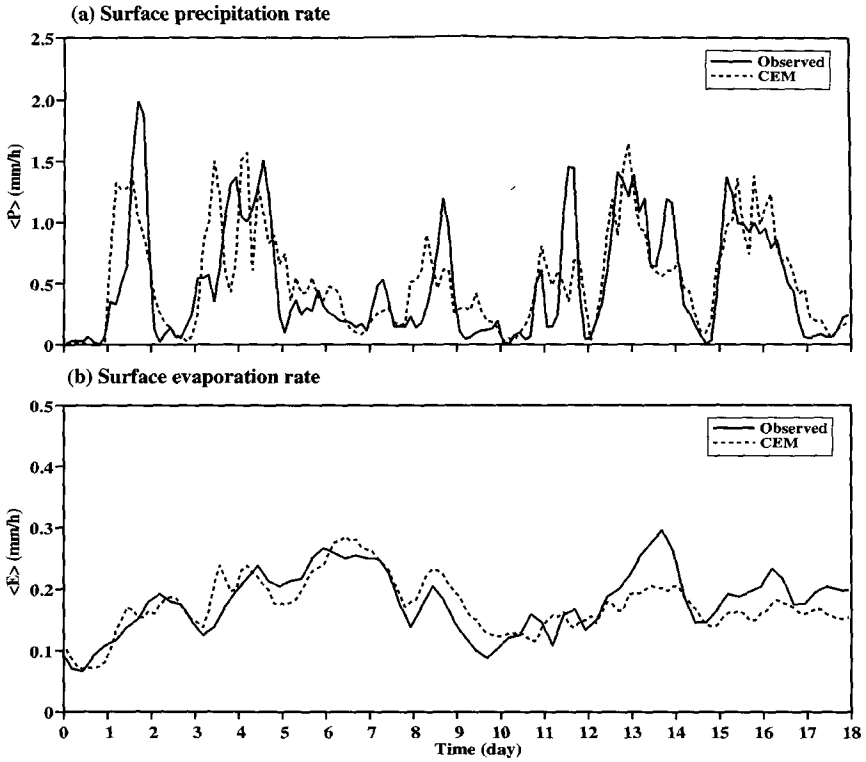

FIG. 12. Time sequence of domain-averaged (a) surface precipitation rate and (b) surface evaporation rate for simulation G and observations.

respectively. Simulated moisture is also mostly lower than observed in the first 9 days but mostly higher in the last 9 days. There is no moistening trend in the model because there are also negative differences in the lowest 3 km and above 5 km of the last 9 days. Again, the model produces statistically significant errors at selected levels during some periods (compare with Fig. 3b).

The large-scale relative humidity is shown in Fig. 14 to further illustrate the difference between simulation and observation because of small values of water vapor mixing ratio in the upper troposphere. The observations are based on the Ooyama dataset. The RH values above 10 km should be treated with caution because they were extrapolated. Below 10 km, simulated RHs agree with observed mostly within 10% except for the first day of the simulation. The small difference between observed and simulated RHs is not surprising because the profiles of temperature and water vapor mixing ratio are strongly coupled in the presence of convection (Arakawa and Chen 1987). This will be further discussed later.

Figure 15a shows the time series of the observed and simulated precipitable water, which is the vertical integral of water vapor mixing ratio over the entire column of the atmosphere. Although the time series of the simulated precipitable water does not agree well with observations, the absolute difference is less than 10% at any given time. In other words, the model does not produce variability of the precipitable water similar to that observed. As discussed in section 4a, depressed convection is not well simulated on selected days. This is further illustrated by Fig. 15b, which shows the vertical integrals of the cloud water and cloud ice mixing ratios. The time variations of cloud water content are rather small in spite of the large variations of the surface precipitation rate, especially between 4 and 9 September (Fig. 12a). On the other hand, the cloud ice content does show large variations. It does not, however, become zero when there is no observed convection (e.g., 10–11 and 15 September). Unfortunately, there are no observations with which to evaluate the time variation of simulated cloud water and cloud ice contents.

The instabilities of the observed and simulated atmospheres (Fig. 15c) are compared with a generalized convective available potential energy (GCAPE), following the computational procedure of Wang and Randall (1994). Figure 15c shows that the time variation of the simulated GCAPE agrees well with the observed except for initial large variations, which may represent a transient adjustment of the simulated convection. As shown earlier, there is little convection on 1 and 3 September when GCAPEs are accumulated.

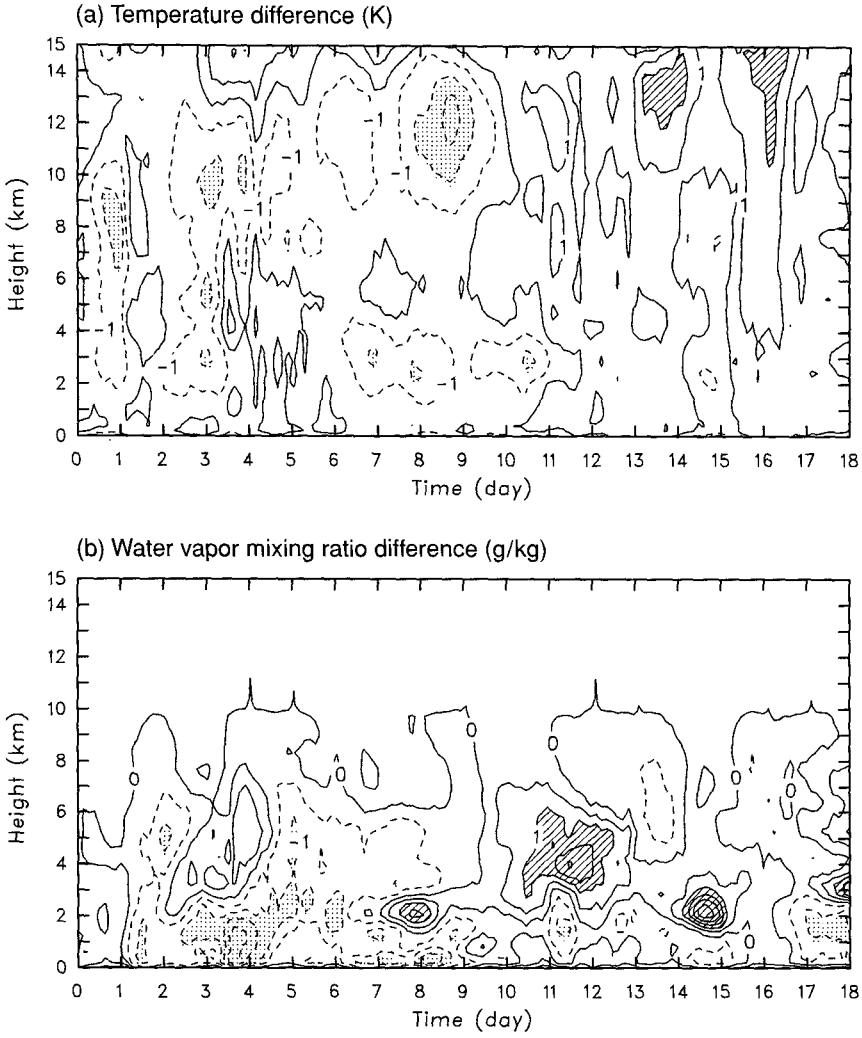

FIG. 13. Time–height cross sections of (a) the temperature difference and (b) the water vapor mixing ratio difference between simulation G and observations. The contour interval is 1 K in (a) and 0.5 g kg^{-1} in (b). Contours over 2 K (1 g kg^{-1}) are hatched. Contours less than −2 K (−1 g kg^{-1}) are dotted.

This is also indicated by the large negative temperature differences shown in Fig. 13a, which favor larger GCAPEs than observed (Wang and Randall 1994). Once convection begins, GCAPE is rather quickly consumed by convection (in 6–9 h). The small GCAPEs after 4 September indicate the quasi-balance between the supply by large-scale processes and the consumption by cumulus convection. After 13 September, the GCAPE of the simulated atmosphere is smaller than observed because the temperature difference is mostly positive in the upper troposphere (Fig. 13a). Nevertheless, the most significant result related to the GCAPE is the almost identical correlation coefficients between GCAPE and surface precipitation rate from the simulation (−0.41) and the observations (−0.43; Wang and Randall 1994). A similar result was obtained by Thompson et al. (1979) in terms of CAPE.

Next, the whole-sky camera observations of cloud amounts for selected layers (Holle et al. 1979) are also compared with the CEM results. Figure 16 shows the daily mean of cloud amounts for selected layers. The observed cloud amounts are averaged over the daytime only (Holle et al. 1979). Missing data at some observation times are excluded in the average. This often happens to the middle-, high- and upper-level cloud amounts. The observed upper-level cloud amount is the difference between the total and low-level cloud amounts (Holle et al. 1979). The CEM results are averaged over the entire domain in space and over 24 h in time. The criterion used for detecting the cloudiness

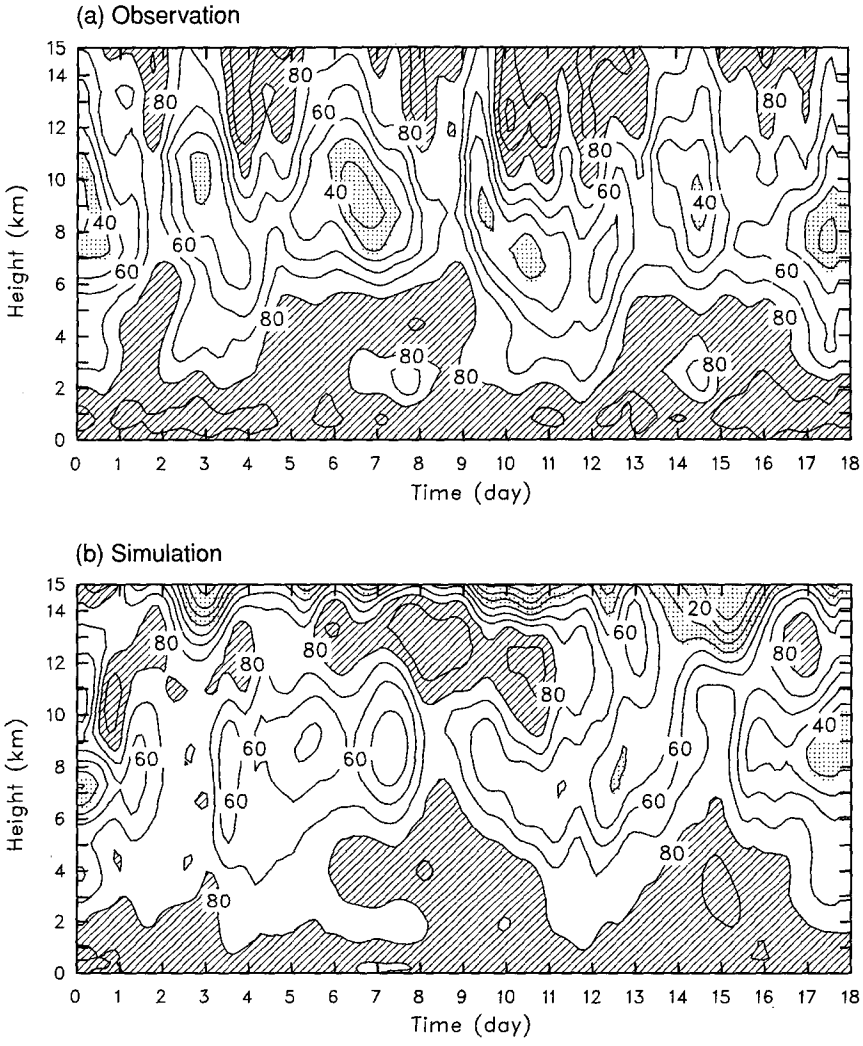

FIG. 14. Same as in Fig. 13 except for (a) the observed and (b) simulated relative humidity. The contour interval is 10%. Contours over 80% are hatched. Contours less than 40% are dotted.

within a layer of a CEM column is that the liquid water (cloud water, cloud ice, and snow) path exceeds 0.01 kg m^{-2} multiplied by the ratio of the layer mass to the total mass of a CEM column.

As seen from Fig. 16, the time evolutions of the amounts of all cloud types are somewhat consistent with the observations except for the smaller amplitudes of the daily fluctuations. The total cloud amount averaged over the Phase III is slightly less than observed. The low-level cloud amount is, however, well underestimated, which is partly related to 1) the neglect of rainwater in defining cloudiness, 2) the model's coarse horizontal resolution and the lack of a subgrid cloudiness parameterization; and 3) possibly the overestimate in the observations due to uncertainty in estimating the cloud base heights. Use of the total condensate mixing ratio for defining the cloudiness produces total cloud amounts more comparable to the observed (not shown). The amounts of the other three cloud types are higher than those observed mainly because the whole-sky camera observations could not observe these cloud types if low-level clouds were present (Holle et al. 1979). Therefore, the simulated amounts are much higher than observed, especially for the high- and upper-level cloud amounts.

A comparison between the time series of the observed and simulated OLRs is shown in Fig. 15d. The observed OLR is based on Murakami (1979) for the B-scale array. The overall agreement between observed and simulated OLRs is good. Significant differences are, however, present on 9 and 15 September, respectively. The 9 September case is related to the abundant upper-level clouds (Fig. 7), which are produced by the large horizontal-advective cooling (Fig. 5a). The 15 September case may be partly due to the presence of upper-level clouds after deep convection dissipates.

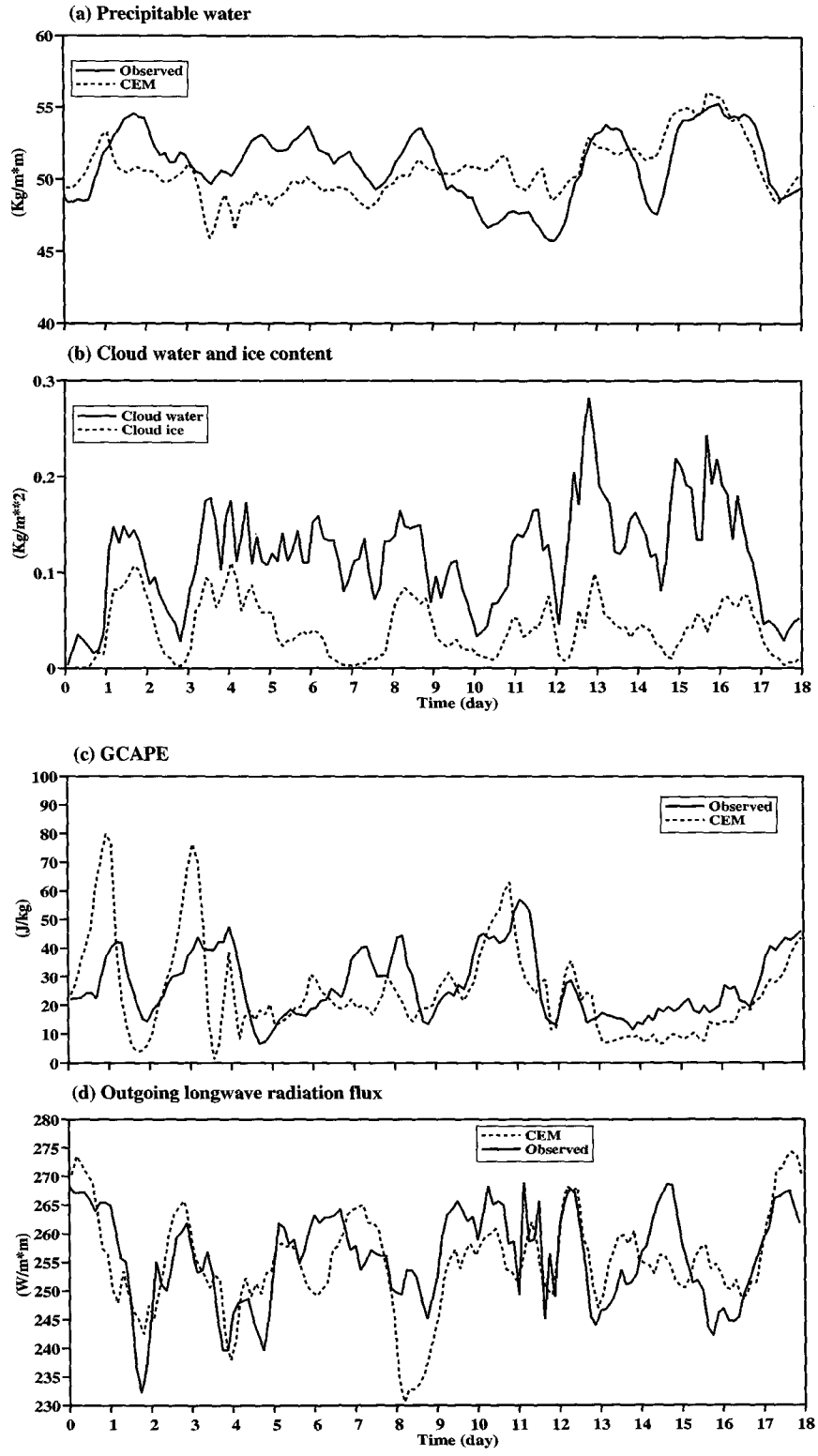

FIG. 15. Time sequence of domain averaged (a) precipitable water, (b) cloud water and cloud ice content, (c) generalized convective available energy, and (d) outgoing longwave radiation flux from simulation G and observations except for (b).

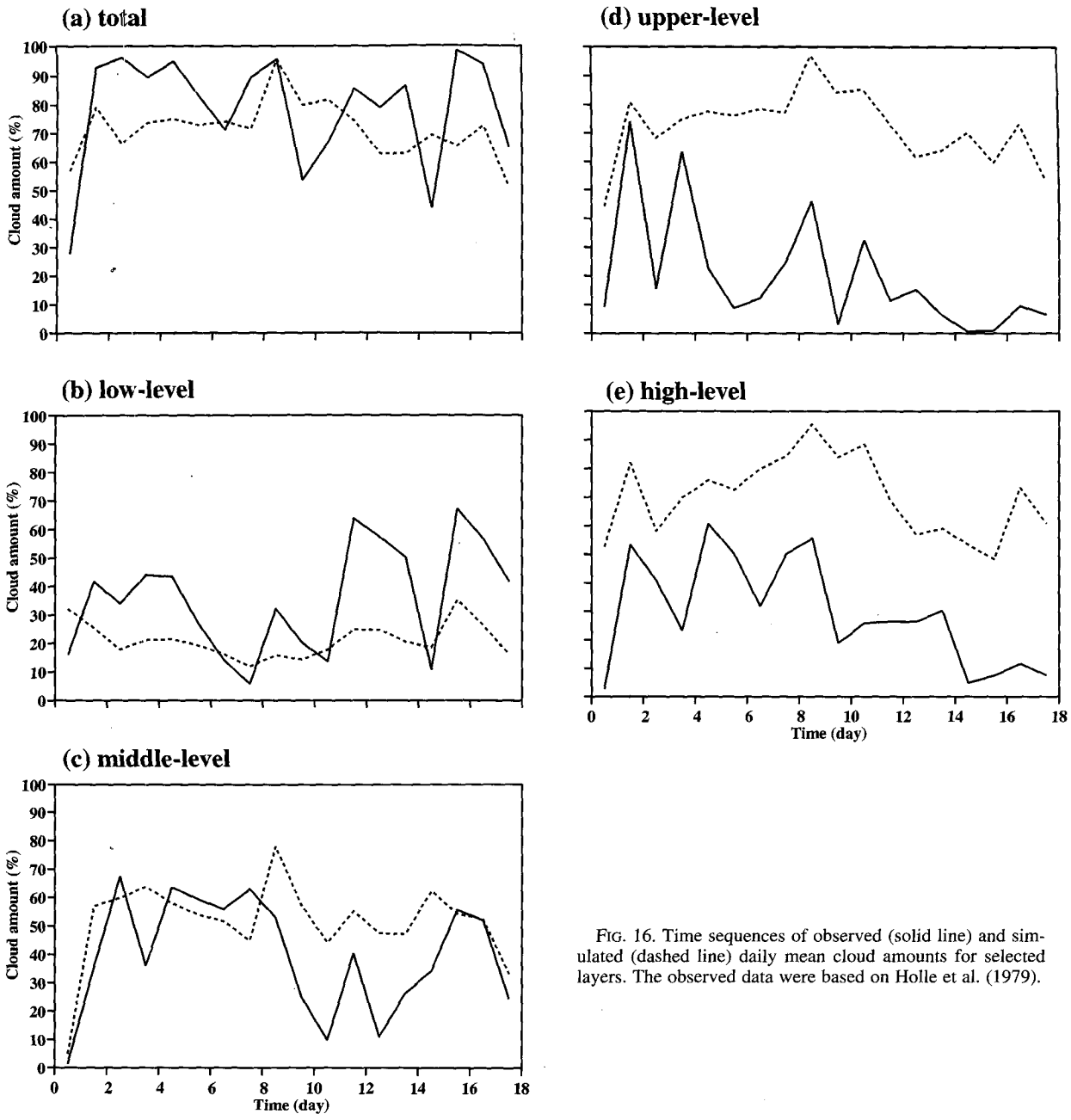

FIG. 16. Time sequences of observed (solid line) and simulated (dashed line) daily mean cloud amounts for selected layers. The observed data were based on Holle et al. (1979).

That is, upper-level clouds do not dissipate quickly in the model due to, for example, the zero falling speed for cloud ice and possibly the lack of cloud ice sink because of the periodic lateral boundary condition. Another reason is that there is sufficient large-scale subsidence to suppress convection during 15 September (Fig. 4c).

Figure 17 shows a comparison of the time series of the simulated and estimated radiative heating rates Q_R (Cox and Griffith 1979). The simulated and estimated Q_R generally agree with each other. Some differences are, however, apparent. For example, the maximum cooling centers of the simulated Q_R appear at higher levels than the estimate. The heating at the daytime extends to much lower levels than the estimate. Nevertheless, the absolute differences between simulated and estimated Q_R are mostly less than 0.5 K day^{-1}. The estimated Q_R for 18 September were not available.

c. *Sensitivity tests*

Figure 18 shows the time sequences of selected variables as in Figs. 12 and 15 for the control (G) and

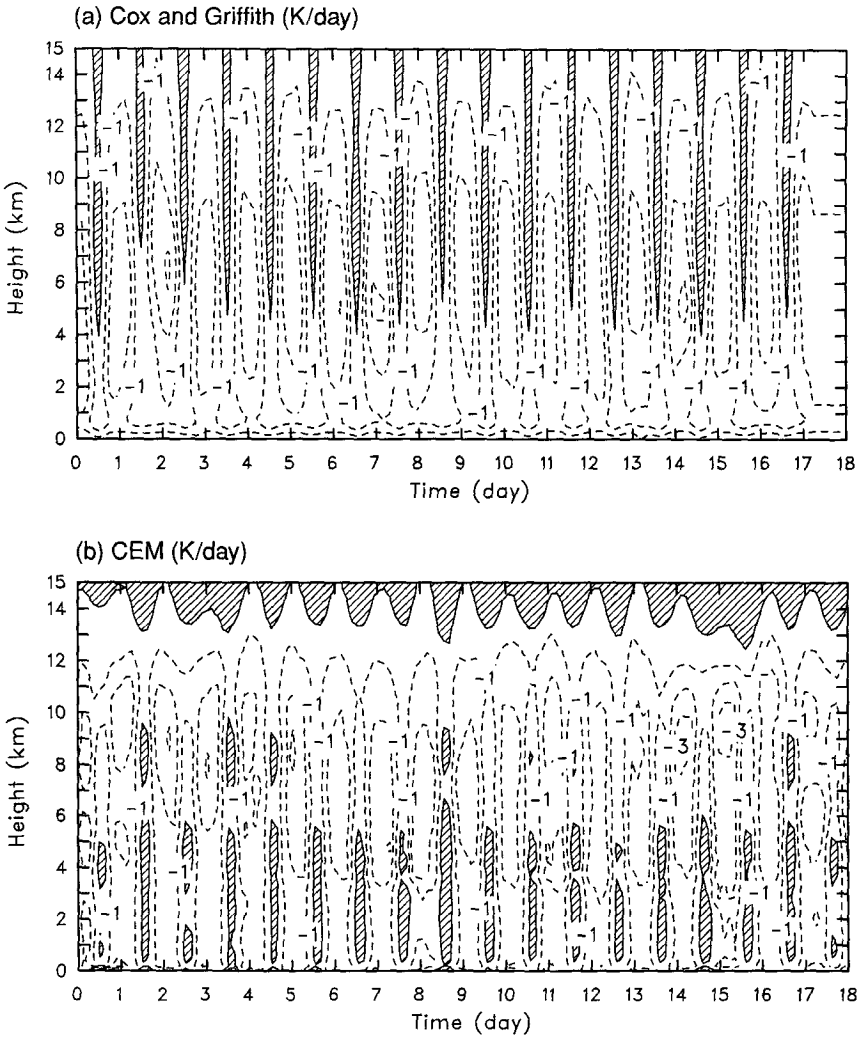

FIG. 17. Time–height cross sections of (a) estimated and (b) simulated radiative heating rates. The contour interval is 1 K day^{-1}. Hatched are contours over 0 K day^{-1}.

sensitivity tests (T and S). The differences between G and T are generally insignificant except for 4 September when the amplitude of diurnal variation of SST is large. Convection starts 2–3 h later than in G in the early morning when the SST is lower than the daily mean, and convection is better sustained in the afternoon (Figs. 18a,e) when the SST is higher than the daily mean (Fig. 2). As convection is delayed, the GCAPE continues to accumulate (Fig. 18f) due to advective cooling in the middle troposphere (Fig. 19a). The differences between G and T on the other five days are weakly influenced by the diurnal variations of SST; that is, there is a somewhat positive correlation between SST and the intensity of convection (Figs. 18a,d, f). At any rate, the comparison between G and T indicates that large amplitudes of SST variation can have significant impact on the intensity of convection. Thus simulated convection between 10 and 16 September in G could agree better with the observations if the observed diurnally varying SST were used.

The differences between G and S are, as expected, much more significant because of the inhibiting effect of vertical wind shear on convection (e.g., Rotunno et al. 1988; Xu et al. 1992). The peak magnitudes of surface precipitation rate on 2 and 4 September are not as high as in G (Fig. 18a). This is because convection starts earlier and there is a smaller accumulation of GCAPE (Fig. 18f) before convection begins. The smaller initial GCAPE inhibits the occurrence of intense convection such as on the early 4 September in G because large-scale advective processes have stronger control on the intensity of convection in S. Xu et al. (1992) investigated the response of cumulus activity to prescribed large-scale forcing. They found that convection is more strongly controlled by large-scale forcing when the wind shear is weak. At any rate, the

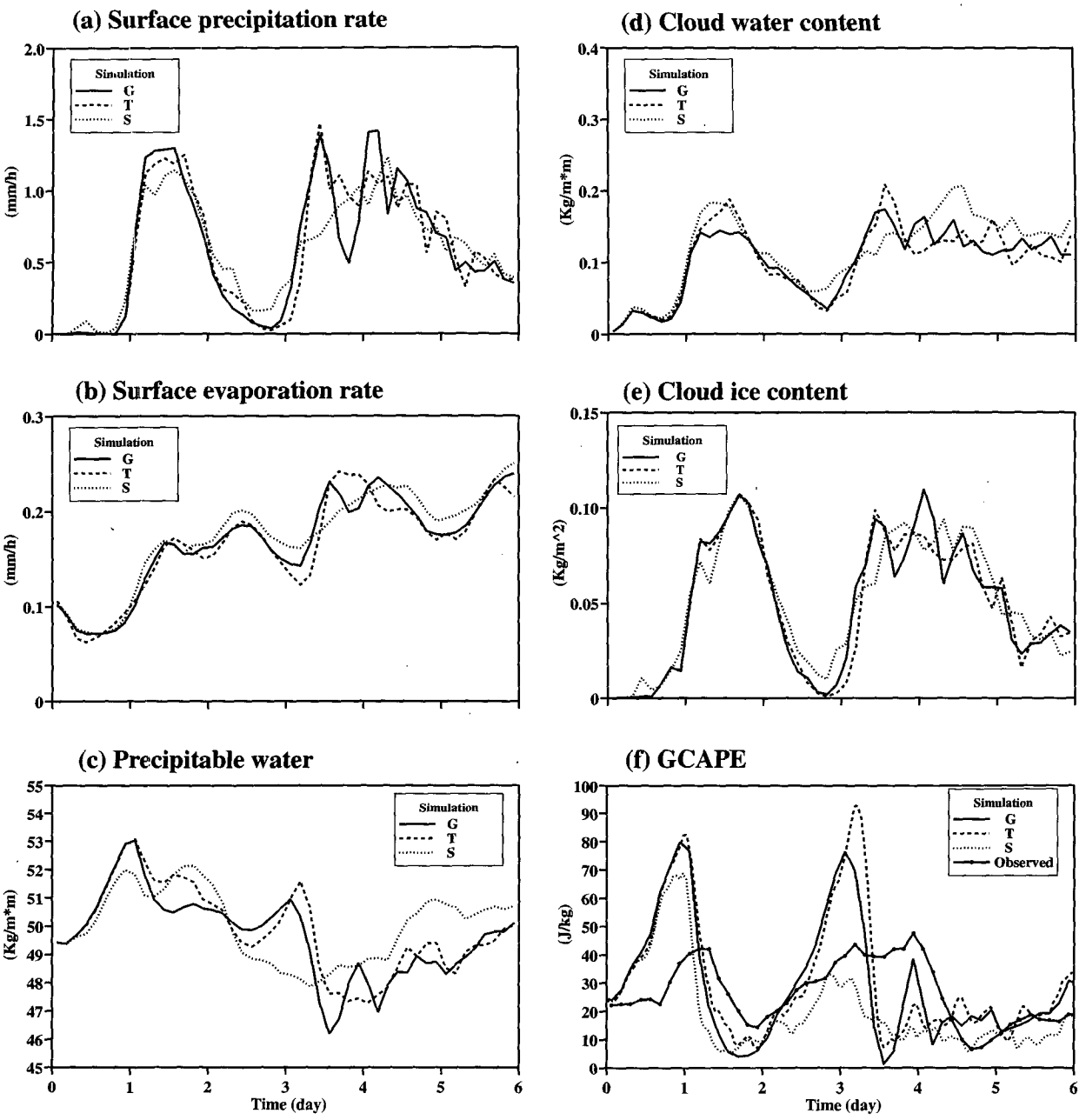

FIG. 18. Time sequences of selected variables (as in Figs. 12 and 15) from the control (G) and sensitivity tests T and S.

surface precipitation rate in S agrees better with the observations than in G on 4 September, so do temperature and moisture between 3 and 4 September (Figs. 19c and 19d). This suggests that the 2D CEM has somewhat stronger inhibiting effects on convection than the observed due to the presence of vertical shear of horizontal wind. This inhibiting effect has a relatively strong impact on cloud water content, precipitable water (Figs. 18c,d), and the lower-level moisture (Fig. 19d).

The large differences between simulation S and G can be more clearly seen from the differences of temperature and water vapor mixing ratio (Figs. 19c and 19d). The atmosphere simulated by S on 3–4 September is warmer and drier than that of G, that is, much more stable. This is also closer to observed (Fig. 13). The moisture between 1 and 5 km is higher in S between 4 and 6 September, and this is also closer to observed. This is probably because less organized convection is far less efficient in transporting moisture up-

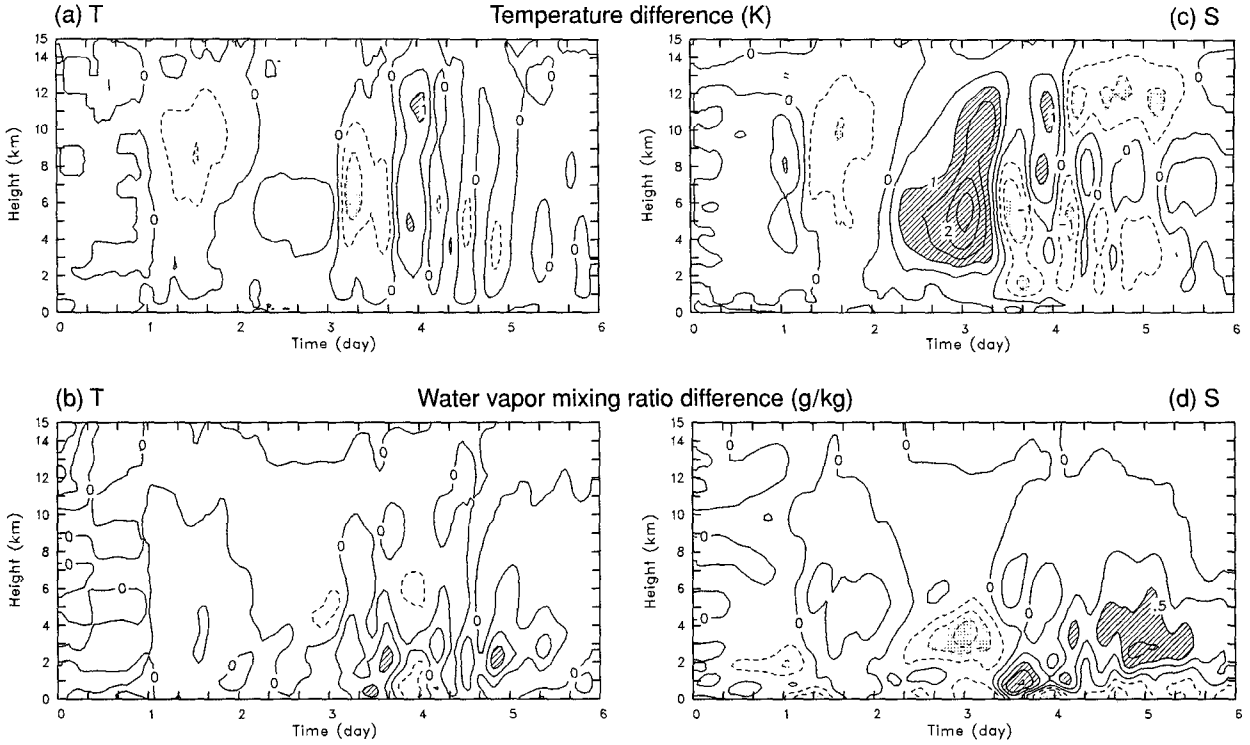

FIG. 19. Time–height cross sections of temperature differences and water vapor mixing ratio differences between sensitivity tests (T and S) and G. The contour interval is 0.5 K in (a) and (c) and 0.25 g kg^{-1} in (b) and (d). Contours over 1 K (0.5 g kg^{-1}) are hatched. Contours less than -1 K (-0.5 g kg^{-1}) are dotted.

ward. In other words, 2D convection may transport moisture far more efficiently than observed in the presence of strong wind shear. No existing cumulus parameterization will respond to the shear at all. This is an important area for future research.

The differences between CT and G are very systematic, due to a higher availability of moisture from the sea surface. First, the 18-day mean surface evaporation is increased by 8%, but the surface precipitation rate is only increased by 6%. In terms of absolute value, the increase in surface precipitation rate is more than twice as great as for the surface evaporation rate. Second, there is the increase of moisture in the lower and middle troposphere (Fig. 20b) and there is a warming of more than 1 K in the middle and upper troposphere (Fig. 20a) throughout simulation CT except for the first few days. (The nonzero difference on 1 September is due to the use of a perturbed initial sounding in this single run.) In other words, the atmosphere is more stable even though the lower and middle troposphere are more moist. The magnitude of the warming in the middle and upper troposphere is constrained by some kind of balance between the stability and moisture, such as that proposed by Arakawa and Chen (1987), so that there is no runaway warming. Another indication of this is that the negative correlation between GCAPE and surface precipitation rate in CT is almost the same as in G. Nevertheless, the comparison between CT and G suggests that the UCLA CEM cannot produce a warming/moistening trend due to the presence of internal constraints. The large temperature differences between G and observations are more likely related to the deficiencies in the Thompson et al. dataset. This point is discussed below.

Figure 21 shows the temperature and water vapor mixing ratio differences between simulation O and observations. Compared with Fig. 13, it is obvious that the simulation with the Ooyama dataset is better than G. That is, the general agreement between simulation O and observations is far better than that between G and observations. The differences between O and G (not shown) are statistically significant. The negative temperature differences between G and observations in the upper troposphere between 8 and 10 September disappear. This confirms that there are errors in the horizontal advective tendency of the upper troposphere in the Thompson et al. dataset (Fig. 5a). The magnitudes of other negative temperature differences are also significantly reduced. The negative moisture differences in the lower troposphere are generally reduced or eliminated. This is related to the small horizontal advective tendency of the lowest 2–3 km in the Thompson et al. dataset (Fig. 5b) and possibly the different methods for prescribing the large-scale vertical advective effect.

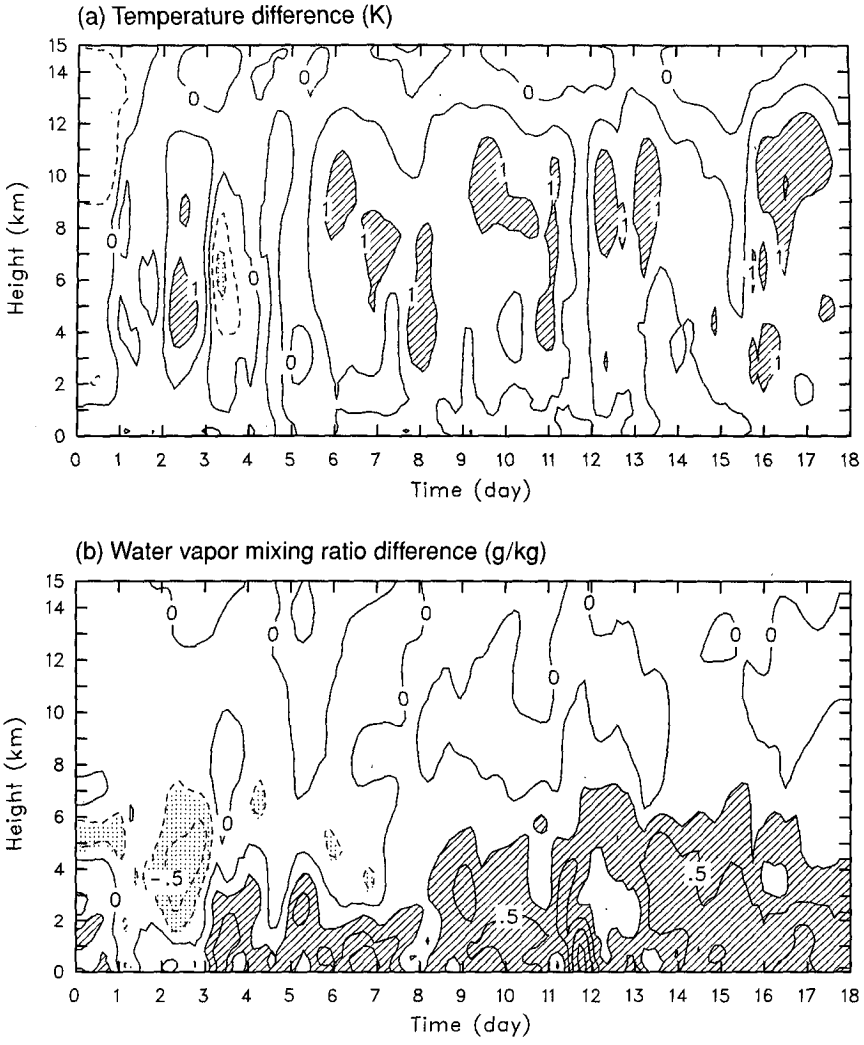

FIG. 20. Same as in Fig. 19 except for the differences between CT and G. The contours over 0.25 g kg^{-1} are hatched in (b).

The latter needs further investigation. In addition, the magnitudes of the overestimates of moisture during some periods are significantly reduced.

Because the design of simulation O is almost identical to that of Grabowski et al. (1996), a comparison with the results in Grabowski et al. (1996) can serve as an intercomparison between CEMs. Further comparison between the different methods in prescribing the large-scale advective effects should be performed in order to determine which method is more appropriate for intercomparison between CEMs. This issue must be addressed by the ongoing GCSS intercomparison project.

5. Summary and discussion

The time evolution of the macroscopic behavior of cumulus convection and its mesoscale organization that occurred during Phase III of GATE has been simulated with a two-dimensional cloud ensemble model (CEM). A series of experiments has been performed with slightly perturbed initial conditions. In this study, the observed large-scale horizontal advective effects and the large-scale vertical velocity are imposed on the model's thermodynamic equations uniformly in the horizontal. The simulated, domain-averaged horizontal wind components are nudged toward the observed winds. A comprehensive comparison with available observations has been made.

The detailed spatial structure and temporal evolution of simulated cloud systems have a fairly good correspondence with observations. The fast-moving mesoscale convective systems (MCSs) appear to be more successfully simulated by the 2D CEM than the slow-moving MCSs because the low-level wind shear is parallel to the direction of propagation of the fast-moving

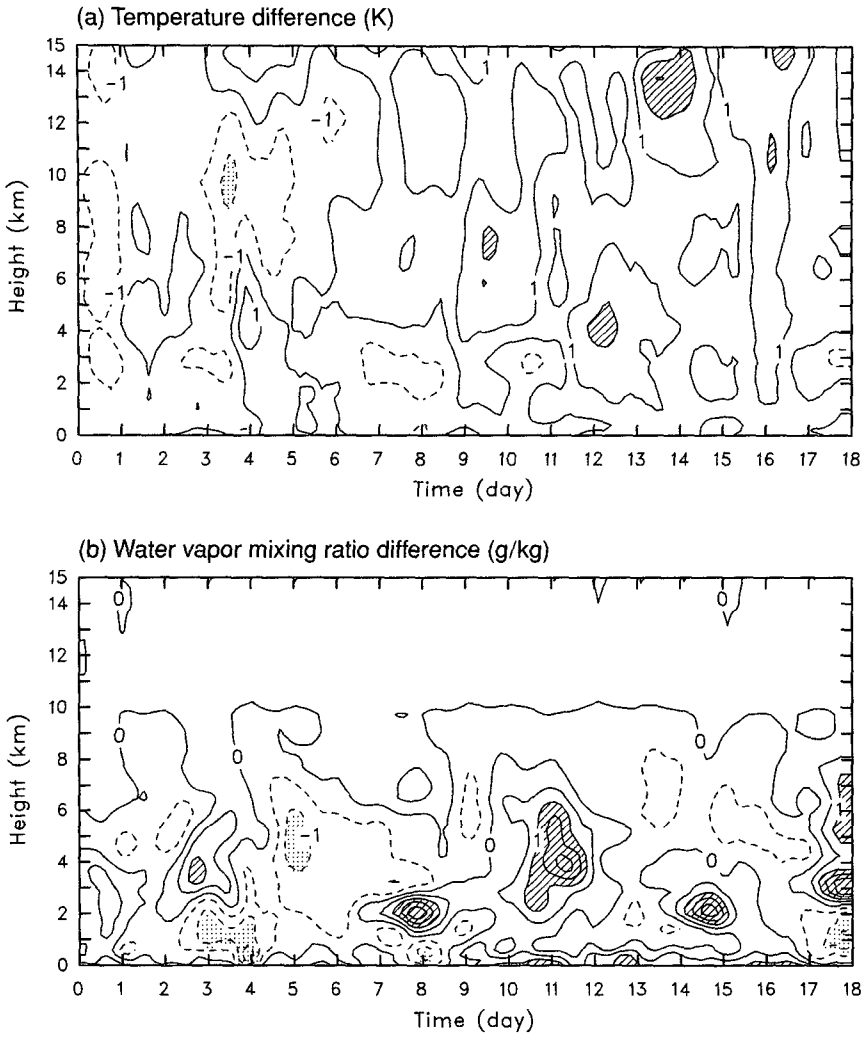

FIG. 21. Same as in Fig. 13 except for simulation O.

MCSs in the 2D setting. The vertical structures of dynamic and thermodynamic characteristics of fast-moving MCSs are extremely similar to observed (e.g., Zipser 1969, 1977; Houze 1977; Gamache and Houze 1982, 1985). Although some thermodynamic aspects of slow-moving MCSs are well simulated, the 2D model cannot simulate their orientation and structures well because the low-level wind shear cannot be normal to the direction of propagation. That is, the 2D model produces somewhat organized convection in the weakly sheared environment, but far less organized than observed because this type of MCSs exhibit three-dimensional structures. The observed multiple cloud systems on 2, 5, and 11 September are not well simulated either.

The observed temporal variations of the surface precipitation rate, surface evaporation rate, precipitable water, outgoing longwave radiative flux, and the vertical distributions of temperature, water vapor mixing ratio, large-scale relative humidity, and the radiative heating rate are successfully reproduced by the model. Some of these variables are more successfully reproduced than the others. The most important and encouraging result presented in this study is that the model is able to reproduce the negative correlation between the intensity of convection and the convective available potential energy. Such an internal constraint prevents the model from producing a warming/moistening trend even when the prescribed SST is systematically higher than observed.

The temporal evolution of the low-level cloud amount and the total cloud amount is comparable with that of the whole-sky camera observations of Holle et al. (1979). The low-level cloud amount is, however,

significantly underestimated. Middle-, high-, and upper-level cloud amounts are also comparable with the observations. The underestimate of low-level clouds is due to a combination of reasons, one of which is due to the model's failure to produce subgrid-scale shallow cumuli without a subgrid cloudiness parameterization (e.g., Sommeria and Deardorff 1977; Mellor 1977) and another is its coarse horizontal resolution.

Major deficiencies of the control simulation include (i) the large temperature differences in the upper troposphere and large moisture differences in the lower troposphere, (ii) the smaller amplitudes of the daily fluctuations such as in the precipitable water, cloud water content and cloud amounts. These two aspects can be largely explained by the insufficient quality of the Thompson et al. dataset because a simulation with the Ooyama dataset does provide a far better agreement between simulation and observations. The Ooyama data set adopted a scale-controlled objective analysis. The second aspect may also be related to shortcomings of the microphysics parameterization and the periodic lateral-boundary conditions.

Other deficiencies of the simulation are related to the limitations of the 2D model. For example, sensitivity tests reveal that 2D model has stronger inhibiting effects on convection and more efficient in vertical transports than observed when the vertical shear of horizontal wind is strong.

In summary, this study has demonstrated that the CEM can successfully simulate the statistical properties of cumulus ensembles for a long period of 18 days. The results are compared favorably with a variety of observations. Some deficiencies of the simulation are present due to the limitations of the 2D CEM.

Acknowledgments. This research was primarily supported by the Environmental Sciences Division of U.S. Department of Energy under Grant DE-FG03-95ER61968 as part of the Atmospheric Radiation Measurement Program. It was also partially supported by CERES under Grant NAG1-1266 and FIRE under Grant NAG1-1701, both from NASA to the Colorado State University.

Observational datasets used in the present study were kindly provided by Professor R. Reed of the University of Washington and Professor M. Yanai of UCLA for the GATE sounding data, and Mr. R. Holle of NOAA NSSL for the whole-sky cloudiness data. We thank Professor Steve Krueger of the University of Utah and Professor Steve Esbensen of Oregon State University for their helpful discussions regarding the simulation and observational dataset, respectively. We are grateful to three anonymous reviewers for their constructive comments.

REFERENCES

Arakawa, A., and W. H. Schubert, 1974: Interaction of a cumulus cloud ensemble with the large-scale environment, Part I. *J. Atmos. Sci.*, **31,** 674–701.

——, and J.-M. Chen, 1987: Closure assumptions in the cumulus parameterization problem. *Short- and Medium-range Numerical Prediction, Collection of Papers at the WMO/IUGG Numerical Weather Prediction Symp.*, Tokyo, Japan, World Meteor. Org. and Int. Union of Geodesy and Geophysics, 107–131.

Arkell, R., and M. Hudlow, 1977: *GATE International Meteorological Radar Atlas.* Environmental Data Service, NOAA, 222 pp. [Available from the Superintendent of Documents, U.S. Government Printing Office, Washington, DC, 20402; Stock No. 003-019-00038-1.]

Barnes, G. M., and K. Sieckman, 1984: The environment of fast- and slow-moving tropical mesoscale convective cloud lines. *Mon. Wea. Rev.*, **112,** 1782–1794.

Betts, A. K., and M. J. Miller, 1986: A new convective adjustment scheme. Part II: Single column tests using GATE wave, BOMEX, ATEX and arctic airmass data sets. *Quart. J. Roy. Meteor. Soc.*, **112,** 692–709.

Cheng, M.-D., 1989a: Effects of downdrafts and mesoscale convective organization on the heat and moisture budgets of tropical cloud clusters. Part I: A diagnostic cumulus ensemble model. *J. Atmos. Sci.*, **46,** 1517–1538.

——, 1989b: Effects of downdrafts and mesoscale convective organization on the heat and moisture budgets of tropical cloud clusters. Part II: Effects of convective-scale downdrafts. *J. Atmos. Sci.*, **46,** 1540–1564.

——, and M. Yanai, 1989: Effects of downdrafts and mesoscale convective organization on the heat and moisture budgets of tropical cloud clusters. Part III: Effects of mesoscale convective organization. *J. Atmos. Sci.*, **46,** 1566–1588.

——, and A. Arakawa, 1990: Inclusion of convective downdrafts in the Arakawa–Schubert parameterization. Tech. Rep., 69 pp. [Available from Department of Atmospheric Sciences, UCLA, Los Angeles, CA 90095.]

Cox, S. K., and K. T. Griffith, 1979: Estimates of radiative divergence during Phase III of the GARP Atlantic Tropical Experiment. Part II: Analysis of Phase III results. *J. Atmos. Sci.*, **36,** 586–601.

Esbensen, S. K., and K. Ooyama, 1983: An objective analysis of temperature and relative humidity data over the B and A/B ship arrays during Phase III of GATE. Oregon State University, Corvallis, Oregon, 87 pp. [Available from College of Oceanic and Atmospheric Sciences, Oregon State University, Corvallis, OR 97331.]

Gallus, W. A., Jr., and R. H. Johnson, 1991: Heat and moisture budgets of an intense midlatitude squall line. *J. Atmos. Sci.*, **48,** 122–146.

Gamache, J. F., and R. A. Houze Jr., 1982: Mesoscale air motions associated with a tropical squall line. *Mon. Wea. Rev.*, **110,** 118–135.

——, and ——, 1985: Further analysis of the composite wind and thermodynamic structure of the 12 September GATE squall line. *Mon. Wea. Rev.*, **113,** 1241–1259.

GCSS Science Team 1993: The GEWEX cloud system study (GCSS). *Bull. Amer. Meteor. Soc.*, **74,** 387–400.

Grabowski, W. W., X. Wu, and M. W. Moncrieff, 1996: Cloud resolving modeling of tropical cloud systems during Phase III of GATE. Part I: Two-dimensional experiments. *J. Atmos. Sci.*, **53,** 3684–3709.

Gregory, D., and M. J. Miller, 1989: A numerical study of the parameterization of deep tropical convection. *Quart. J. Roy. Meteor. Soc.*, **115,** 1209–1241.

Harshvardhan, R. Davies, D. A. Randall, and T. G. Corsetti, 1987: A fast radiation parameterization for general circulation models. *J. Geophys. Res.*, **92,** 1009–1016.

Holle, R. L., J. Simpson, and S. W. Leavitt, 1979: GATE B-scale cloudiness from whole-sky cameras on four U.S. ships. *Mon. Wea. Rev.*, **107,** 874–895.

Houze, R. A., Jr., 1977: Structure and dynamics of a tropical squall-line system. *Mon. Wea. Rev.*, **105,** 1540–1567.

——, 1982: Cloud clusters and large-scale vertical motions in the tropics. *J. Meteor. Soc. Japan,* **60,** 396–410.

——, and A. K. Betts, 1981: Convection in GATE. *Rev. Geophys. Space Phys.*, **19,** 541–576.

Hudlow, M. D., and V. L. Patterson, 1979: GATE radar rainfall atlas. NOAA Special Report, U.S. Govt. Printing Office, Washington, D.C., 155 pp. [Available from Superintendent of Documents, U.S. Govt. Printing Office, Washington, DC 20402; Stock No. 003-019-00046-2.]

International Council of Scientific Unions and World Meteorological Organization (ICSU/WMO), 1972: Experimental design proposal for the GARP Atlantic Tropical Experiment. GATE Rep. 1, 188 pp. [Available from Secretariate of the WMO, Case Postale No. 1, CH-1211, Geneva 20, Switzerland.]

Johnson, R. H., 1976: The role of convective-scale precipitation downdrafts in cumulus and synoptic-scale interactions. *J. Atmos. Sci.*, **33,** 1890–1910.

——, and G. S. Young, 1983: Heat and moisture budgets of tropical mesoscale anvil clouds. *J. Atmos. Sci.*, **40,** 2138–2147.

Krishnamurti, T. N., V. Wong, H. L. Pan, G. van Dam, and D. McClellan, 1976: Sea surface temperatures for GATE. Rep. 76-3, Department of Meteorology, The Florida State University, 268 pp. [Available from Department of Meteorology, The Florida State University, Tallahassee, FL 32306.]

——, Y. Ramanathan, H.-L. Pan, R. J. Pasch, and J. Molinari, 1980: Cumulus parameterization and rainfall rates I. *Mon. Wea. Rev.*, **108,** 465–472.

Krueger, S. K., 1988: Numerical simulation of tropical cumulus clouds and their interaction with the subcloud layer. *J. Atmos. Sci.*, **45,** 2221–2250.

——, Q. Fu, K. N. Liou, and H.-N. Chin, 1995: Improvements of an ice-phase microphysics parameterization for use in numerical simulations of tropical convection. *J. Appl. Meteor.*, **34,** 281–287.

Kuettner, J. P., and D. E. Parker, 1976: GATE: Report on the field phase. *Bull. Amer. Meteor. Soc.*, **57,** 11–27.

Kuo, H. L., 1965: On formation and intensification of tropical cyclones through latent heat release by cumulus convection. *J. Atmos. Sci.*, **22,** 40–63.

——, 1974: Further studies of the parameterization of the influence of cumulus convection on large-scale flow. *J. Atmos. Sci.*, **31,** 1232–1240.

Leary, C. A., 1979: Behavior of the wind field in the vicinity of a cloud cluster in the Intertropical Convergence Zone. *J. Atmos. Sci.*, **36,** 631–639.

——, and R. A. Houze Jr., 1979: The structure and evolution of convection in a tropical cloud cluster. *J. Atmos. Sci.*, **36,** 437–457.

——, and ——, 1980: The contribution of mesoscale motions to the mass and heat fluxes of an intense tropical convective system. *J. Atmos. Sci.*, **37,** 784–796.

LeMone, M. A., G. M. Barnes, and E. J. Zipser, 1984a: Momentum flux by lines of cumulonimbus over the tropical oceans. *J. Atmos. Sci.*, **41,** 1914–1932.

——, ——, E. J. Szoke, and E. J. Zipser, 1984b: The tile with height of the leading edge of a tropical mesoscale convective line. *Mon. Wea. Rev.*, **112,** 510–519.

Lin, Y.-L., R. D. Farley, and H. D. Orville, 1983: Bulk parameterization of the snow field in a cloud model. *J. Climate Appl. Meteor.*, **22,** 1065–1092.

Lipps, F. B., and R. S. Hemler, 1986: Numerical simulation of deep tropical convection associated with large-scale convergence. *J. Atmos. Sci.*, **43,** 1796–1816.

Lord, S. J., 1982: Interaction of a cumulus cloud ensemble with the large-scale environment. Part III: Semi-prognostic test of the Arakawa–Schubert cumulus parameterization. *J. Atmos. Sci.*, **39,** 88–103.

——, H. E. Willoughby, and J. M. Piotrowicz, 1984: Role of a parameterized ice-phase microphysics in an axisymmetric, nonhydrologic tropical cyclone model. *J. Atmos. Sci.*, **41,** 2836–2848.

Manabe, S., J. Smagorinsky, and R. F. Strickler, 1965: Simulated climatology of a general circulation model with a hydrologic cycle. *Mon. Wea. Rev.*, **93,** 769–798.

Mansfield, D. A., 1977: Squall lines observed during GATE. *Quart. J. Roy. Meteor. Soc.*, **103,** 569–574.

Mellor, G. L., 1977: The Gaussian cloud model relations. *J. Atmos. Sci.*, **34,** 356–358.

Mower, R. N., 1977: Case study of convection lines during GATE. Atmospheric Science Paper No. 271, Colorado State University, Fort Collins, Colorado, 92 pp. [Available from Department of Atmospheric Science, Colorado State University, Fort Collins, CO 80523.]

Murakami, M., 1979: Large-scale aspects of deep convective activity over the GATE area. *Mon. Wea. Rev.*, **107,** 994–1013.

National Research Council (NRC), 1980: Proceedings, *Seminar on the Impact of GATE on Large-Scale Numerical Modeling of the Atmosphere and Ocean,* Woods Hole, MA, NRC, 276 pp.

Ogura, Y., and H.-R. Cho, 1973: Diagnostic determination of cumulus populations from large-scale variables. *J. Atmos. Sci.*, **30,** 1276–1286.

Ooyama, K., 1987: Scale-controlled objective analysis. *Mon. Wea. Rev.*, **115,** 2476–2506.

Ostapoff, F., 1977: B/C-scale oceanography. *Report of the U.S. GATE Central Program Workshop,* NCAR, 407–440.

Randall, D. A., K.-M. Xu, R. C. J. Somerville, and S. Iacobellis, 1996: Single-column models and cloud ensemble models as links between observations and climate models. *J. Climate,* **9,** 1683–1697.

Rotunno, R., J. B. Klemp, and M. L. Weisman, 1988: A theory for strong, long-lived squall lines. *J. Atmos. Sci.*, **45,** 463–485.

Sommeria, G., and J. W. Deardorff, 1977: Subgrid-scale condensation in models of nonprecipitating clouds. *J. Atmos. Sci.*, **34,** 344–355.

Soong, S.-T., and W.-K. Tao, 1980: Response of deep tropical cumulus clouds to mesoscale processes. *J. Atmos. Sci.*, **37,** 2016–2034.

Stephens, G. L., S.-C. Tsay, P. W. Stackhouse Jr., and P. J. Flatau, 1990: The relevance of the microphysical and radiative properties of cirrus clouds to climate and climate feedback. *J. Atmos. Sci.*, **47,** 1742–1753.

Sui, C.-H., and M. Yanai, 1986: Cumulus ensemble effects on the large-scale vorticity and momentum fields of GATE. Part I: Observational evidence. *J. Atmos. Sci.*, **43,** 1618–1642.

Tao, W.-K., and S.-T. Soong, 1986: A study of the response of deep tropical clouds to mesoscale processes: Three-dimensional numerical experiments. *J. Atmos. Sci.*, **43,** 2653–2676.

——, J. Simpson, and S.-T. Soong, 1987: Statistical properties of a cloud ensemble: A numerical study. *J. Atmos. Sci.*, **44,** 3175–3187.

——, ——, C.-H. Sui, B. Ferrier, S. Lang, J. Scala, M.-D. Chou, and K. Pickering, 1993: Heating, moisture and water budgets of tropical and midlatitude squall lines: Comparisons and sensitivity to longwave radiation. *J. Atmos. Sci.*, **50,** 673–690.

Thompson, R. M., Jr., S. W. Payne, E. E. Recker, and R. J. Reed, 1979: Structure and properties of synoptic-scale wave disturbances in the introtropical convergence zone of the eastern Atlantic. *J. Atmos. Sci.*, **36,** 53–72.

Wang, J., and D. A. Randall, 1994: The moist available energy of a conditionally unstable atmosphere. Part II: Further analysis of GATE data. *J. Atmos. Sci.*, **51,** 703–710.

Webster, P. J., and G. L. Stephens, 1980: Tropical upper troposphere extended clouds: Inferences from Winter MONEX. *J. Atmos. Sci.*, **37,** 1521–1541.

Xu, K.-M., 1995: Partitioning mass, heat and moisture budgets of explicitly simulated cumulus ensembles into convective and stratiform components. *J. Atmos. Sci.*, **52,** 551–573.

——, and S. K. Krueger, 1991: Evaluation of cloudiness parameterizations using a cumulus ensemble model. *Mon. Wea. Rev.*, **119,** 342–367.

——, and A. Arakawa, 1992: Semiprognostic tests of the Arakawa–Schubert cumulus parameterization using simulated data. *J. Atmos. Sci.*, **49,** 2421–2436.

——, and D. A. Randall, 1995a: Impact of interactive radiative transfer on the macroscopic behavior of cumulus ensembles. Part I: Radiation parameterization and sensitivity test. *J. Atmos. Sci.*, **52,** 785–799.

——, and ——, 1995b: Impact of interactive radiative transfer on the macroscopic behavior of cumulus ensembles. Part II: Mechanisms for cloud-radiation interactions. *J. Atmos. Sci.*, **52,** 800–817.

——, A. Arakawa, and S. K. Krueger, 1992: The macroscopic behavior of cumulus ensembles simulated by a cumulus ensemble model. *J. Atmos. Sci.*, **49,** 2402–2420.

Yanai, M., and R. H. Johnson, 1993: Impacts of cumulus convection on thermodynamic fields. *The Representation of Cumulus Convection in Numerical Models, Meteor. Monogr.*, No. 46, Amer. Meteor. Soc. 39–62.

——, S. Esbensen, and J.-H. Chu, 1973: Determination of bulk properties of tropical cloud clusters from large-scale heat and moisture budgets. *J. Atmos. Sci.*, **30,** 611–627.

Zipser, E. J., 1969: The role of organized unsaturated convective downdrafts in the structure and rapid decay of an equatorial disturbance. *J. Appl. Meteor.*, **8,** 799–814.

——, 1977: Mesoscale and convective-scale downdrafts as distinct components of squall-line structure. *Mon. Wea. Rev.*, **105,** 1568–1589.

——, R. J. Meitin, and M. A. LeMone, 1981: Mesoscale motion fields associated with a slowly moving GATE convective band. *J. Atmos. Sci.*, **38,** 1725–1750.